

HST/NICMOS IMAGING POLARIMETRY OF PROTO-PLANETARY NEBULAE II: MACRO-MORPHOLOGY OF THE DUST SHELL STRUCTURE VIA POLARIZED LIGHT

TOSHIYA UETA¹, KOJI MURAKAWA², MARGARET MEIXNER³

To appear in the Astronomical Journal

ABSTRACT

The structure of the dusty circumstellar envelopes (CSEs) of proto-planetary nebulae (PPNs) reveals the mass-loss history of these sources and how such histories may differ for elliptical (SOLE) and bipolar (DU- PLEX) PPNs. To study the PPN structures via dust-scattered linearly polarized starlight, we have compiled the imaging-polarimetric data for all 18 evolved stars that have been obtained to date with NICMOS on-board the *Hubble Space Telescope* (*HST*). This alternative imaging technique provides a unique way to probe the distribution of dust grains that scatter light around evolved stars. The new perspective gained from the imaging-polarimetric data has revealed several new aspects to the structures of PPNs. Point-symmetry is a prevalent imaging-polarimetric characteristic resulting from the azimuthal density gradient in the CSEs. Among these point-symmetric nebulae, three detailed morphological types can be differentiated by their polarized intensity, I_p , and polarization strength, P . While the azimuthal density gradient is reversed above and below the equatorial plane in optically thicker bipolar nebulae, there is no gradient reversal in optically thinner elliptical nebulae. The equatorial plane of the system defined by the integrated angle of polarization is not necessarily orthogonal to the axis of the apparent bipolar structure in the total intensity data.

Subject headings: circumstellar matter — stars: AGB and post-AGB — stars: individual (IRAS z02229+6208, IRAS 04296+3429, IRAS 04395+3601, IRAS 06530–0213, IRAS 07134+1005, IRAS 09452+1330, IRAS 10131+3049, IRAS 10178–5958, IRAS 10197–5750, IRAS 12419–5414, IRAS 16594–4656, IRAS 17150–3224, IRAS 17245–3951, IRAS 17423–1755, IRAS 17441–2411, IRAS 19343+2926, AFGL 2688) — stars: mass loss — reflection nebulae

1. INTRODUCTION

Proto-planetary nebulae (PPNs; e.g. Kwok 1993; Van Winckel 2003) are low to intermediate initial mass ($\sim 1 - 8 M_{\odot}$) objects that are rapidly becoming planetary nebulae (PNs) after evolving off the asymptotic giant branch (AGB). A PPN consists of a post-AGB central star and a circumstellar envelope (CSE) of gas and dust that is created by mass loss from the central star during the AGB phase. When mass loss ceases at the end of the AGB phase, the CSE physically detaches from the central star and keeps coasting away during the PPN phase. Thus, PPNs preserve the AGB mass-loss history imprinted in the density distribution of the CSEs. Therefore, PPNs are the best astrophysical laboratories in which we investigate the nature of dusty mass loss during the AGB phase.

During the last decade, high-resolution imaging observations have revealed a plethora of morphologies among PNs and PPNs (see review by Balick & Frank 2002). One of the most important tasks in the AGB stellar research is therefore to determine the main physical factors that cause such a great morphological diversity emerging from AGB mass-loss geometry, which is highly spherically symmetric at the beginning of the AGB phase (e.g. Habing & Blommaert 1993). The observed morphological diversity suggests a number of shell shaping processes, and various mechanisms have been proposed to explain the observed morphologies (Balick & Frank

2002, and references therein). In all possible cases, however, the CSE structure must deviate from the initial spherical symmetry. Therefore, there may exist a universal mechanism through which the required symmetry breaking is achieved, and thus, we have been performing surveys to identify the mechanisms that generate the initial non-sphericity in the CSEs of AGB stars.

Using mid-IR ($8 - 21 \mu\text{m}$) data, Meixner et al. (1999) have shown that all the extended PPNs in their sample are axisymmetric and fall into one of the two morphological classes: toroidal (showing limb-brightened peaks that suggest the presence of a dusty torus) or core/elliptical (showing an unresolved emission core surrounded by a low surface brightness elliptical nebula). They concluded that the last stage of AGB mass loss is short-lived and inherently toroidal (i.e., equatorially-enhanced), probably coinciding with a period of enhanced mass loss known as the “superwind” phase (Renzini 1981; Iben & Renzini 1983).

In an optical imaging survey of PPN candidates using the Hubble Space Telescope (*HST*), Ueta et al. (2000) have detected elongated reflection nebulosities whose morphologies appear to bifurcate depending on the degree of the equatorial density enhancement in the CSE. SOLE (Star-Obvious Low-level Elongated) PPNs show a bright central star embedded in a faint, elliptically-elongated nebulosity, while DUPLEX (DUst-Prominent Longitudinally EXtended) PPNs exhibit a remarkable bipolar structure with a dust lane completely or partially obscuring the central star. These optical morphological classes appear to possess a one-to-one correspondence to the mid-IR counterparts (core/elliptical \approx DUPLEX and toroidal \approx SOLE).

Subsequent radiative transfer modeling of some selected sources (e.g. Meixner et al. 1997; Ueta et al. 2001b;

¹ Department of Physics and Astronomy, University of Denver, Denver, CO 80208, USA; tueta@du.edu

² Max-Planck-Institut für Radioastronomie, Auf dem Hügel 69, G-53121, Bonn, Germany

³ Space Telescope Science Institute, 3700 San Martin Drive, Baltimore, MD 21218, USA

Meixner et al. 2002, 2004) have shown that (1) the observed PPN axisymmetry emerges during a brief stage of an enhanced mass loss ($\sim 3 \times 10^{-5} M_{\odot} \text{ yr}^{-1}$) towards the end of the AGB phase, (2) the enhanced mass-loss rate into the equatorial plane is very much higher ($\gtrsim 10^3$) than that into the polar directions, and (3) the differences between SOLE and DUPLEX PPNs stem from the physical distinction between the two types and cannot be attributed solely to the inclination angle effects. Furthermore, it appears that SOLE and DUPLEX PPNs develop respectively from low and high mass progenitors. This agrees with a recent discovery of mostly bipolar structures among OH/IR-selected sources, which are located close to the galactic plane (i.e., more massive), observed by *HST* (Sahai & Sánchez Contreras 2004).

Imaging polarimetry is an alternative technique to probe the CSE structure, in which the dust-scattered linearly polarized component of light can be separated from the unpolarized component of light. Gledhill and collaborators (Gledhill et al. 2001; Gledhill 2005) have found, through UKIRT imaging-polarimetric surveys of PPN candidates, that the axisymmetric structure of the PPN shells fall into one of the two classes, *shell* and *bipolar*, depending on the amount of dust in the CSE. These classes respectively correspond to SOLE and DUPLEX PPNs. The results of the previous mid-IR and optical surveys have thus been confirmed.

We have performed near-IR imaging polarimetry with *HST* to investigate the dust distribution in SOLE PPNs by making use of the polarized intensity (I_p) maps. Imaging polarimetry is especially powerful for this purpose, because the technique isolates dust-scattered light arising from the CSE and permits us to probe the CSE structure even in the vicinity of the bright central star; CSE structure is often obscured in total intensity (I) maps, which are affected by the enormous point-spread-function (PSF) of the central star. Since I_p depends only on the Stokes Q and U , which are free from the unpolarized component by definition, it can be extracted even from the PSF-affected data. We have successfully demonstrated that (1) SOLE PPNs consist of a hollow spheroidal shell which has a built-in equatorial density enhancement and (2) the variable degree of the equatorial density enhancement (i.e., the optical depth of the CSE) would result in a variety of apparent PPN structure even among this specific group of optically thin PPNs (Ueta et al. 2005, hereafter Paper I).

In the present work, we extend our investigation of the CSE structure via I_p into the realm of DUPLEX PPNs. We apply the technique of imaging polarimetry in investigating the structure of the *bipolar lobes*, in which the optical depth is generally low enough for the method to work. To date, there have been observations of 18 evolved stars by *HST*/NICMOS in the polarimetric mode. Only a small portion of the entire data set has been published, and the I_p data have rarely been utilized to study the CSE dust distribution. Therefore, we analyze all the existing *HST*/NICMOS imaging polarimetric data, especially in I_p , obtained from the archive in order to obtain more insights into the general mechanism(s) responsible for the structure development in the AGB wind shells. Below, we describe the data set and reduction procedure briefly (§2), present and discuss the results both individually and in groups (§3) and give a summary (§4).

2. OBSERVATIONS AND DATA REDUCTION

We have collected NICMOS imaging-polarimetric data for 13 evolved stars from the *HST* archive and combined them with our own data for 4 SOLE PPNs that have already been

published (Paper I). When PSF correction is necessary, we have used data for two PSF calibration sources, HD 12088 and BD+32°3739, respectively in the NIC1 and NIC2 band. Table 1 summarizes the major observing parameters for all observations. Unfortunately, the data for IRAS 02168 and IRAS 10131 (in the POL-L band) are affected by severe saturation and not included in the subsequent analysis. In the following, we use the IRAS designation of the targets to refer to each object except for AFGL 2688, which does not have an IRAS designation.

The standard set of NICMOS pipeline routines, CALNICA (Version 3.1), in IRAF/STSDAS⁴ has been used in data reduction. Additional care has been taken to remove the pedestal effect (a variable quadrant bias) and the Mr. Staypuft (the amplifier ringing and streaking due to bright targets; Dickinson et al. 2002). When multiple frames are combined, we have used the drizzle package (Koekemoer et al. 2002) in STSDAS. The resulting images maintain their original pixel scales of $0''.043 \text{ pixel}^{-1}$ and $0''.075 \text{ pixel}^{-1}$ respectively in the NIC1 and NIC2 band.

Derivation of the Stokes parameters is done via the matrix inversion method (Hines et al. 2000; Dickinson et al. 2002). However, the coefficients are different for data taken before and after the servicing mission 3B (SM3B) in 2002 March, during which the NICMOS cooling system was installed. This resulted in two sets of the photometric conversion factors for the pre- and post-SM3B data. We have used these coefficients (listed in Table 2 of Paper I) where appropriate. A more detailed account of data reduction is found in Paper I.

3. RESULTS AND DISCUSSION

3.1. Results

The imaging-polarimetric maps of evolved stars are presented in a uniform format, following the scheme in Paper I (Figs. 1 to 14: Readers are encouraged to look at the color images available on the electronic version of the paper.). In each figure, we show (a) the total intensity, I , map, (b) the polarized intensity, I_p , map, (c) the polarization strength, P , map and (d) the polarization vector position angle (P.A.), θ , map, respectively from top to bottom. When the PSF-subtracted data are available, they are also displayed in the right column (panels e–h) in addition to the original data in the left panels, except for IRAS 10131 and AFGL 2688 for which the two-epoch data are presented (the earlier/later epoch on the left/right).

The results are also summarized in Table 2, which lists the measured coordinates and I and I_p fluxes of the object, the maximum P (P_{\max}), the mean P ($\langle P \rangle$) and its standard deviation, and description of the I_p structure. The listed coordinates are the center of the polarization vector pattern that is determined by minimizing the sum of the square of the distance from the presumed center to a line orthogonal to the polarization vectors. The pattern center is initially assumed to be the I peak (when seen), and the center finding process is iterated until the shift between the previous and current centers becomes smaller than the numerical accuracy of the analysis. The fluxes are determined by integrating the surface brightness over an aperture in which there is more than one σ_{sky} detection. P_{\max} and $\langle P \rangle$ plus its standard deviation are determined by using an aperture which is delineated by the

⁴ IRAF is distributed by the NOAO, which is operated by AURA under cooperative agreement with NSF. STSDAS is a product of STScI, which is operated by AURA for NASA

well-established nebula edge or an aperture in which there is more than three σ_{sky} detection. The I_p structure is described by the overall shape, dimensions (typically major and minor axis lengths), and P.A. measured from the north to the east.

To compare the present results with the previous unresolved polarization measurements, we have also performed aperture polarimetry and summarized the results with the measurements of Paper I in Table 3. We have done aperture photometry on the three polarizer images and then used the measured fluxes from each polarizer image to compute the integrated P and θ . We have varied the aperture size from $\times 1$ to $\times 8$ of FWHM in I to determine how the resulting values of P and θ behave as a function of the aperture size. In general, P and θ become stable and converge to a single value when the aperture size is equal to or larger than five times the FWHM size in I . Thus, the aperture size is defined to be the minimum aperture size (an integer multiple of FWHM in I) over which the integrated P and θ are generally stable. The quoted errors in P (0.2 to 4.0%) and θ (at most 6°) are thus the maximum deviation in our measurements when the aperture size is varied beyond the adopted aperture size. These values are consistent with the results of more thorough analyses done by Hines et al. (2000)⁵ and Batcheldor et al. (2006)⁶.

We have adopted the integrated θ as a measure of the orientation of the equatorial plane because of the following reason. When the optical depth in the equatorial region is very high ($\tau \gg 1$), there is little I_p because of the dilution effects due to multiple scattering. In this case, the integrated θ tends to be parallel to the equatorial plane because of the orthogonal alignment of the scattering plane with respect to the equatorial plane (e.g., Whitney & Hartmann 1993; Gledhill 2005). However, when the optical depth is marginally high (~ 1), θ in the equatorial region can be orthogonal to the equatorial plane due to scattering at the walls of the bipolar lobes (e.g., Johnson & Jones 1991; Trammell et al. 1994; Gledhill 2005; Oppenheimer et al. 2005). Even in this case, the integrated θ tends to be parallel to the equatorial plane, because vectors in the lobes away from the equatorial region would still dominate. Therefore, the integrated θ is more appropriate as a measure of the orientation of the equatorial plane, and is expressed as θ_{eq} in the following. Note, however, that θ_{eq} is defined to be the angle perpendicular to the orientation of the equatorial plane so that the comparison between θ_{eq} and P.A. of the I_p surface brightness distribution can be done intuitively.

3.2. Individual Sources

3.2.1. IRAS 04395+3601 (AFGL 618)

IRAS 04395 (Fig. 1) is a DUPLEX PPN that is on the verge of becoming a PN (Westbrook et al. 1975; Calvet & Cohen 1978). The I map shows its well known bipolar structure elongated in the east-west direction due to multiple outflows (Trammell, & Goodrich 2002). The lobe interior structure is more clearly revealed in the I map than in recent high-resolution ground-based near-IR maps (Ueta et al. 2001a). PSF subtraction did not improve the quality of the data because no post-SM3B PSF data with a comparable degree of saturation is available and the whole PSF structure (especially of the spikes) is enlarged due to the bright, extended emission

⁵ In verifying the matrix coefficients by measuring polarization of both polarized and unpolarized standards, their measurements were consistent within 0.3% in P and 5° in θ

⁶ Possible instrumental polarization would make the matrix coefficients uncertain and was found to cause difference of 0.1% in P and 3° in θ .

core.

The I_p map shows a general bipolar shape of the nebula superposed by clumpy structures in the lobes, as has been revealed in the optical by Trammell, & Goodrich (2002). However, we do not see the tips of the outflows in I_p . This is consistent with their shock-excited nature (Ueta et al. 2001a). The morphology of the nebula changes dramatically in the P map. Strong polarization is localized in several clumps distributed along the south edge of the west lobe and the north edge of the east lobe (respectively marked as W and E clumps in Fig. 1c). These clumps are distributed along a curve that delineates an inverse S. The θ map shows general centrosymmetry, and the vector pattern center and the I peak are roughly coincident.

The structure of the lobes in I_p and P suggests that there is more dust on one side of the lobe than the other, given that the lobes are optically thin at near-IR. The regions of enhanced surface brightness in I_p and P spatially correspond to the shortest of the multiple outflows seen in $H\alpha$ (Trammell, & Goodrich 2002)⁷. This indicates that these regions of enhanced local density are associated with the latest outflows that channel recently ejected matter away from the central region, provided that mass loss proceeds at a constant velocity. In fact, θ_{eq} (83°) is aligned with the directions of these most recent outflows delineated by strong I_p and P ($\sim 85^\circ$), and is not aligned with the bipolar axis (94°). This implies that the current orientation of the equatorial dust torus is oblique with respect to the bipolar axis (by about 10°).

The clumpiness in the outflow structures of the enhanced I_p and P surface brightness suggests mass loss that is episodic. Trammell, & Goodrich (2002) have shown multiple ring-like structures in $H\alpha$ and [S II] emission as well as an arc in $H\alpha$ silhouette. These structures are in line with the episodic mass loss interpretation. These clumps, however, could alternatively imply instabilities in the outflows, as pointed out also by Trammell, & Goodrich (2002).

Provided that outflows are associated with episodic mass ejection, the angular separation between clumps corresponds to the interval of mass ejection. The separations between clumps are $1''.1$ and $1''.3$ in the west lobe respectively for the first and second closest clump pairs from the central star, and $0''.9$ in the east lobe. Using 120 km s^{-1} outflow velocity (Trammell, & Goodrich 2002) and the distance of 1.7 kpc (Bujarrabal et al. 1988) and assuming a linear outflow, these separations translate to 60 to 90 years. Given the uncertainty in the exact geometry of the outflows and of the clumps, these values are reasonably close to the value of 40 years (scaled to our choice of the distance) derived by Trammell, & Goodrich (2002) based on the separation between the ring-like structures seen in $H\alpha$ and [S II].

3.2.2. IRAS 09452+1330 (IRC +10 216)

IRAS 09452 (Fig. 2) is one of the brightest thermal IR sources in the sky (Becklin et al. 1969), and hence, one of the best-studied C-rich AGB star. The CSE (of DUPLEX type) is seen as a fragmented bipolar nebula having four major emission components in the optical and near-IR (Skinner et al. 1998; Osterbart et al. 2000; Tuthill et al. 2000; Weigelt et al. 2002; Murakawa et al. 2005).

⁷ The east clumps correspond to the eastern outflow “d” (the northernmost of the three outflows), while the west clumps coincide with the shortest western outflow (the southernmost outflow in the west) as presented in Figure 1 of Trammell, & Goodrich (2002).

The I map shows the main nebulosity that is stretched at a P.A. of 22° . We recognize three fragments in the north (marked as the “NE”, “N”, and “NW” in Fig. 2a respectively from east to west [P.A. = 22° , -19° , & -66°]; Osterbart et al. 2000; Tuthill et al. 2000; Weigelt et al. 2002) and an arc beyond the south lobe (about $3''$ away from the central peak; Mauron & Huggins 2000).

The I_p map shows the CSE structure more clearly than the I map, but it suffers from the polarization ghosts (high I_p regions located radially with semi-regular intervals in the west and southeast as indicated in Fig. 2; Hines et al. 2000). The northeast and south lobes form the main bipolar nebulae at a P.A. of 22° . However, it is not clear if the north and northwest lobes also have their counterparts in the southeast because of the ghosts. Murakawa et al. (2005) have detected little ($\lesssim 10\%$) polarization in the southeast in recent ground-based imaging polarimetry in the H band and suggested that the north and northwest lobes are caused by leakage of light through fissures in the west side of the central dust torus. The southeast ghosts are more obvious as in the P map. These ghosts are also the source of the anomalous polarization vector pattern in the otherwise centrosymmetric θ map.

Our aperture polarimetry has yielded θ_{eq} of 32° . This is consistent with past polarimetric measurements in the optical through mid-IR (Shawl & Zellner 1970; Dyck et al. 1971; Capps & Dyck 1972; Capps & Knacke 1976; Trammell et al. 1994; Serkowski & Shawl 2001). Therefore, the bipolar lobes are obliquely oriented (10° off) with respect to the equatorial plane. Moreover, the southwest lobe appears larger than the northeast lobe. This is probably due to inclination of the lobes with respect to the plane of the sky: the angle of 20° has been determined based on radiative transfer calculations (Skinner et al. 1998).

3.2.3. IRAS 10131+3049 (CIT 6)

IRAS 10131 (Fig. 3) is an IR-bright C-rich extreme AGB star (Ulrich et al. 1966; Cohen 1979). Schmidt et al. (2002) have studied the CSE structure in detail using a set of *HST* data to show the presence of (1) large IR bipolar lobes (about 10 times larger than in the optical) in the northeast-southwest direction and (2) multiple concentric arcs $1''$ to $4''$ away from the central star. The two-epoch maps in Fig. 3 show the ghosts affecting all the quadrants of the field of view since the roll angle of *HST* at the two epochs differs by about 180° . We do not recognize any internal structure in the CSE core in the I_p and P maps.

A series of IR polarimetry between 1967 and 1976 showed that θ varied between 110° and 180° (Dyck et al. 1971; Kruszewski 1971; Kruszewski, & Coyne 1976). Especially, Kruszewski, & Coyne (1976) reported an IR polarimetric variability on the order of several months. Although Schmidt et al. (2002) have determined that there is no evidence for temporal changes in the polarimetric properties of the CSE structure between the two epochs, there is some 6° change in θ_{eq} . This may be related to the intrinsic IR polarimetric variability of the object. With respect to the measured θ_{eq} values, the shell elongation is not exactly perpendicular (8° to 14° offset). If θ_{eq} varies as θ , it may suggest variations in the dust density distribution near the equatorial plane on the order of months.

3.2.4. IRAS 10178–5958 (Hen 3-401)

IRAS 10178 (Fig. 4) is a PPN of DUPLEX type associated with a Be post-AGB star. *HST* observations in the optical

and H_2 1-0 S(1) bands have revealed this object’s highly collimated structure (García-Lario et al. 1999; Sahai et al. 1999). In the I map we see the collimated bipolar lobes that are linearly elongated into a P.A. of 73° . The equatorial region shows a pinched waist due to extinction. The inner structure in the IR does not appear as sharply as in the optical.

The I_p and P maps clearly reveal the physically thin nature of the walls of the cylindrical lobes. The dust lane that separates both lobes is more clearly delineated. Moreover, I_p and P maps show, in the bipolar “skirt” region, that the northwest and southeast walls are more enhanced than the southwest and northwest walls, respectively. Furthermore, the southwest and northeast walls appear longer than the southeast and northwest walls, respectively. The θ map indicates a rather aligned distribution of polarization angles by a shallow gradient of the image tone over the bipolar lobes (especially away from the central star). Nevertheless, the θ map is generally centrosymmetric centered at the I peak.

Our measurements yield $\theta_{\text{eq}} = 80^\circ$. The P map shows an elliptically elongated region of weak P ($\lesssim 20\%$ at a P.A. of 78°) superposed on the dust lane. This weak P region, therefore, is almost orthogonally oriented with the equatorial plane. This suggests that this weak P region may represent the region of diluted polarization due to starlight leaking through the biconical openings of the dust torus aligned with the equatorial plane. However, the cylindrical lobes are aligned at a P.A. of 73° , which is slanted by 7° with respect to the equatorial plane. In addition, the east end of the northwest wall and the west end of the southeast wall (the regions marked as “enhanced skirt” in Fig. 4c) seem to be slightly curved towards the central star with respect to the rest of the walls, which are very much linear. It appears as if these curved ends of the walls trace the weak P region.

The polarimetric data thus uncover (1) the point-symmetric distribution of scattering matter in the cylindrical lobes (the northwest and southeast walls are more enhanced) and (2) the misalignment between the axes of the equatorial plane and the collimated cylindrical lobes. As a cause for the highly collimated structure of the nebula, García-Lario et al. (1999) on one hand suggested an extreme density contrast within the dust torus that would preferentially channel outflows into spatially-confined regions, while Sahai et al. (1999) on the other proposed a dissipative hydrodynamic interaction of jets with the surroundings. Both scenarios, however, still require additional mechanisms to direct the outflows/jets along the cylindrical lobes that are not orthogonally aligned with the equatorial plane. Alternatively, the enhancements in the northwest and southeast walls of the lobes may be simply due to the illumination effects as suggested from the shape of the weak P region, since the biconical openings of the central dust torus (implied by the orientation of the weak P region) are pointed towards these regions of enhanced I_p and P . The pronounced double-shell structure at the east end of the northwest wall and the west end of the southeast wall may be related to the misalignment.

3.2.5. IRAS 10197–5750 (Hen 3-404)

IRAS 10197 (Fig. 5) is a bipolar DUPLEX nebula surrounding an A2I star that is associated with OH maser emission (Allen et al. 1980). The optical reflection nebulosity has been imaged with *HST* to reveal its butterfly shape (Sahai et al. 1999). The *HST* imaging polarimetric data is generally consistent with the previous imaging polarimetric results presented by Scarrott & Scarrott (1995), but reveal

much more detailed structure.

The I map exhibits some differences in comparison with the optical map. Near-IR light delineates a figure **S** rather than a butterfly shape as in the optical maps, filling the regions of heavy optical extinction such as the equatorial dust lane and the dark “spur” of dust (Sahai et al. 1999). The I_p and P maps reveal the nebula’s point-symmetry better than the I map: polarized light is more concentrated on the east edge of the north lobe and the west edge of the south lobe. The distribution of polarized light emphasizes the figure **S** appearance of the nebula. The θ map shows general centrosymmetry. However, the I peak position does not coincide with the center of the polarization pattern. The location of the central star derived from the polarization pattern is $(\alpha, \delta)_{J2000} = (10^{\text{h}}21^{\text{m}}33^{\text{s}}.88, -58^{\circ}05'47''.7)$.

The θ_{eq} measurement yields 34° . Because of the complexity of the nebula, we can define a number of axes that may characterize the nebula structure as indicated in the I_p map (Fig. 5b). The lobe axis is oriented with a P.A. of (1) 23° based on the overall structure of the polarized nebula, (2) -3° based on the tips of the figure **S** appearance, (3) 67° based on the strongest I_p distribution in the nebula, and (4) -15° based on the protrusions along the western edge of the north lobe and the eastern edge of the south lobe. Furthermore, there is a region of weak P ($\lesssim 20\%$) that is elliptically elongated at the center of the nebula (similar to what has been seen in IRAS 10178). This weak P ellipse is oriented with a P.A. of 12° (indicated in the P map, Fig. 5c).

None of these axes is exactly perpendicular to the equatorial plane. If we assume, as in IRAS 10178, that the orientation of the weak P ellipse corresponds to the direction of the biconical openings of the central dust torus, then the torus is slanted with respect to the equatorial plane. In such a case, the central dust torus needs to precess with roughly 46° to shape the nebula structure by outflows through the biconical openings of the torus.

3.2.6. IRAS 12419–5414 (Boomerang Nebula)

IRAS 12419 is a very large optical bipolar reflection nebula ($55'' \times 21''$; Wegner & Glass 1979), in which very strong optical polarization has been detected (45–60% in the lobes; Taylor & Scarrott 1980). The *HST* data in Fig. 6 show polarization in the central $8'' \times 8''$ region of the nebula at $2\mu\text{m}$. In the I map, we see an extremely faint nebulosity in the PSF-dominated central region, which appears to be shaped in a figure **j** at a P.A. of 0° . Although the nebula is too faint to perform PSF subtraction effectively, the I map shows that the near-IR lobes are elongated along the general north-south direction (slightly tilted along the northwest-southeast quadrants).

The I_p and P maps marginally show the distribution of polarized light along four “streaks” radially emanating from the central region (P.A. of -170° , -55° , 125° , and 10° as indicated in Fig. 6b). These streaks seem to delineate the edges of the bipolar lobes. The θ map pattern appears generally centrosymmetric. Although the degree of polarization is similar in the near-IR and optical around the central star ($12 \pm 8\%$ and 15% , respectively), the polarization angle is not the same (147° and 80° , respectively). This is probably caused by the matter in the equatorial region that is optically thick in the optical but optically thin in the near-IR.

3.2.7. IRAS 16594–4656

IRAS 16594 (Fig. 7) is an evolved post-AGB star associated with a multi-funneled optical reflection nebula, in which shocks start to shape the shell structure (Hrivnak et al. 1999; Van de Steene, & van Hoof 2003). The imaging-polarimetric data of this object have been presented by Su et al. (2003) and us (Paper I). Since this object presents an interesting case of a rather optically thin DUPLEX PPN, we briefly re-describe the structure of the nebula. This object possesses (1) an elliptical nebula elongated in the east-west direction (P.A. of 82°) with an additional protrusion towards northwest (P.A. of -60°) and (2) the bipolar cusps in I_p that delineate the innermost edges of the equatorial density enhancement in the shell. The cusps are spatially coincident with H_2 emission (Hrivnak et al. 2004), which shows enhancements at the edges of the equatorial torus in an otherwise elliptically elongated shell (aligned with one of the optical funnels). P is slightly enhanced on the south edge in the east lobe and on the north edge in the west lobe. The vector pattern is generally centrosymmetric.

θ_{eq} is found to be 22° , which is unrelated to any of the observed structure. While IRAS 16594 is of DUPLEX type based on its shell structure, the fact that the central star is visible in the optical and near-IR suggests that the optical depth in the equatorial region is near the lower limit for DUPLEX (about unity). Moreover, the two-peaked mid-IR core structure found in the equatorial region (García-Hernández et al. 2004) also indicates rather low-density enhancement. Thus, our θ_{eq} measurement may have been affected by the bright PSF.

3.2.8. IRAS 17150–3224

IRAS 17150 (Fig. 8) is an archetypical DUPLEX PPN with a highly equatorially enhanced shell (Meixner et al. 2002 and references therein). The I map reveals the equatorial region of the nebula, which is very much obscured in the optical (Kwok et al. 1998; Ueta et al. 2000). *HST* images in near-IR bands have been presented by Su et al. (2003). From the polarization pattern, we find that the position of the central illumination source is $(\alpha, \delta)_{J2000} = (10^{\text{h}}17^{\text{m}}19^{\text{s}}.81, -32^{\circ}27'21''.2)$, which is $0''.14 \pm 0''.07$ off from the central I peak.

The I_p and P maps display the bipolar structure of the nebula, in which the hollowness of the lobes is highlighted by the polarized light delineating the edges and polar caps. In addition, P is even more strengthened in the north wall of the northwest lobe and in the south wall of the southeast lobe. Thus, there is a preferential distribution of scattering matter in a figure **S**. The measured θ_{eq} is 120° , which is consistent with the bipolar axis at a P.A. of 122° .

3.2.9. IRAS 17245–3951

IRAS 17245 (Fig. 9) is a less studied post-AGB star (Hrivnak et al. 1999), whose less evolved nature has been suggested by the star’s association with OH maser emission (Sevenster 2002). The polarization maps reveal the bipolar nature of the nebula that does not possess an apparent bipolar nebulosity in the total intensity maps (Gledhill et al. 2001; Su et al. 2003). While the main bipolar lobes are oriented along the north-northeast to south-southwest direction, the tail end of the nebula tips appears to be twisted towards opposite directions: the north tip to northwest and the south tip to southeast. This tendency is seen more clearly in the P map, in which the strongly polarized tips are found at a P.A. of 7° . The bipolar axis of the overall nebula elongation is oriented at

a P.A. of 15° , while θ_{eq} is found to be 21° . Thus, there is 6° misalignment between the bipolar axis and the orientation of the equatorial plane.

3.2.10. IRAS 17423–1755 (*Hen 3-1475*)

IRAS 17423 (Fig. 10) is a highly collimated bipolar PPN (of DUPLEX) associated with high velocity outflows (e.g. Sánchez Contreras & Sahai 2001; Riera et al. 2003). The present data cover only part of the brighter northern lobe in the NIC1 band. The I map mainly shows the northwest lobe of the central hourglass-shaped bipolar structure that is inclined with respect to the plane of the sky. The extended knots are seen in the I map (up to the NW2 knot; Riera et al. 2003). The I_p map reveals the physically thin walls of the bipolar lobes more clearly.

Strong polarization is found close to the west side of the north lobe and to the east side of the south lobe (in the central “hourglass” part). These strong P regions are found at a P.A. of -54° (indicated in Fig. 10c). This angle is nearly orthogonal to the equatorial plane ($\theta_{\text{eq}} = 128^\circ$). There is 5° misalignment between the equatorial plane and the general orientation of the bipolar lobes (at a P.A. of 133°). Thus, these strong P regions can be interpreted as the particular locations in the walls of the bipolar lobes that are illuminated by the central star through the biconical openings of the central dust torus, which is not orthogonal to the axis of the bipolar lobes.

3.2.11. IRAS 17441–2411

IRAS 17441 (Fig. 11) is a GOI post-AGB star associated with an optical nebula of DUPLEX type (Su et al. 1998; Ueta et al. 2000). The figure S shape of the nebula is more pronounced in the near-IR than in the optical, as seen in the I map. The I peak coincides with the polarization pattern center, and thus, represents the central source obscured in the optical.

As in IRAS 10197, a number of axes can be defined based on various morphological/polarimetric characteristics. The tips of the figure S shell point to a P.A. of -2° , while the inner region of the nebula, where I_p is the strongest, is elongated along a P.A. of 46° . The P map reveals the walls of the bipolar lobes, which are generally oriented towards a P.A. of 6° . However, the central weak P region ($\lesssim 20\%$) appears elongated along a P.A. of 20° . Aperture polarimetry determines θ_{eq} of 28° , which agrees with none of the characteristic P.A.s described above.

Oppenheimer et al. (2005) have constructed a detailed model of this object using evacuated bipolar lobes with an equatorial disk by fitting their polarization data from optical to near-IR. Their model is quite successful in reproducing the highly polarized nature of the shell as well as the axisymmetric overall geometry of the object. However, their model does not address the point-symmetric aspect of the shell structure. The polarization structure is peculiar in IRAS 17441 because I_p is enhanced in the east edge of the north lobe and the west edge of the south lobe, but P is enhanced in the opposite side in each lobe.

3.2.12. IRAS 19343+2926 (*M 1-92*)

IRAS 19343 (Fig. 12) is an O-rich PN of DUPLEX type, which has been extensively studied (Trammell, & Goodrich 1996; Bujarrabal et al. 1998a,b, and references therein). The bipolar lobes that are separated by the dust lane are seen in the I maps as have been seen in the previous observations in atomic and H_2 line emission (Bujarrabal et al. 1998b) as well as in CO (Bujarrabal et al. 1994, 1998a). We do not see, however, the chains of spots in the bipolar cavities that have been identified as shock-excited clumps of mate-

rial (Bujarrabal et al. 1998b). Their non-detection in scattered light is consistent with their proposed shock-excited nature and suggests very little presence of scattering matter around the shocked gas.

The overall polarization characteristics are generally consistent with the previous optical imaging polarimetry (Schmidt et al. 1978). The present data show that (1) I_p is concentrated in the walls of the bipolar lobes, revealing the hollow nature of the lobes, and (2) strong P is found along the north edge of the northwest lobe and the south edge of the southeast lobe of the nebula that is generally centrosymmetric. The nebula shape defines the symmetric axis (P.A. of 131°), along which CO outflow velocity is found to have an almost constant latitudinal gradient (Bujarrabal et al. 1998a). This axis is, however, not aligned with θ_{eq} of 151° . As in other objects, we find some P enhancements in the nebula along the opposite edges in each lobe.

3.2.13. AFGL 2688 (Egg Nebula)

AFGL 2688 (Figs. 13 and 14) is a DUPLEX PPN that is considered one of the archetypes (Ney et al. 1975; Sahai et al. 1998), and its structure has recently been reviewed in detail by Goto et al. (2002). The I maps show the object's well known bipolar lobes plus the concentric arc structure and the "spindle" structure along the dust lane between the lobes (seen only in the NIC2 band; Fig. 14a). The I_p maps display the point-symmetric nature of the lobes with the brightness enhancement appearing near the southeast corner of the north lobe and near the northwest corner of the south lobe. It is remarkable that the spindle structure has almost zero polarization. This is because the spindle structure is largely in H_2 emission (Cox et al. 1997; Kastner et al. 2001).

In the P maps, strong polarization arises near the northwest corner of the north lobe and near the southeast corner of the south lobe. The equatorial region of the nebula is optically thick even to near-IR light, but optically thin lobes show a generally centrosymmetric pattern in the θ map from which the position of the illumination source is determined (Weintraub et al. 2000). θ_{eq} (17° to 19° P.A.) is slightly misaligned with respect to the axis of the nebula (P.A. of 12° ; Weintraub et al. 2000; Goto et al. 2002). Proper-motion measurements of the shell structure using the two-epoch NICMOS data have yielded the distance of 420 pc to the object (Ueta et al. 2006).

3.2.14. IRAS 07134+1005, 06530-0213, 04296+3429, and (z)02229+6208

Imaging-polarimetric characteristics of these SOLE objects have already been discussed in detail (Paper I). Here, we briefly summarize our findings.

IRAS 07134 (Fig. 3 of Paper I) is a C-rich F5Iab post-AGB star (Hrivnak et al. 1989) associated with an elliptical nebula (Meixner et al. 1997; Dayal et al. 1998; Jura et al. 2000a; Ueta et al. 2000; Kwok et al. 2002). The shell is a slightly prolate spheroid with an inner cavity and a built-in equatorial enhancement, and hence, is not simply "toroidal" as has been interpreted by previous mid-IR observations (Meixner et al. 1997; Dayal et al. 1998; Jura et al. 2000a; Kwok et al. 2002). In addition, the I_p map confirmed that there is more matter on the east side of the nebula than the west (Meixner et al. 2004).

IRAS 06530 (Fig. 4 of Paper I) is a C-rich F5Ib post-AGB star (Hrivnak & Reddy 2003) with an elliptical reflection nebula (Ueta et al. 2000). The nebula is a nearly edge-on prolate spheroid with a possible inner cavity. The nebula's density

structure appears such that the equatorial region of the cavity is filled with some matter, which manifests itself as the density-enhanced bipolar cusp-like structure. However, the total amount of dust along the equator is still not large enough to cause self-extinction within the shell (but close to the upper limit for a SOLE nebula).

IRAS 04296 (Fig. 5 of Paper I) is a C-rich G0Ia post-AGB star (Hrivnak 1995) that is associated with an X-shaped optical elongation (Sahai 1999; Ueta et al. 2000). While Sahai (1999) suggested that these elongations represent a pair of bipolar jets and a collimating disk, we interpreted that the shell had two, most likely hollow, spheroids: one (P.A. of 26°) is nearly edge-on and the other (P.A. of 99°) is inclined with respect to the plane of the sky. The two-spheroid interpretation was favored by a recent dust scattering modeling of the object (Oppenheimer et al. 2005).

IRAS 02229 (Fig. 6 of Paper I) is a C-rich G8-K0Ia post-AGB star (Hrivnak, & Kwok 1999) surrounded by an elliptical nebula of dust-scattered starlight (Ueta et al. 2000) and dust emission (Kwok et al. 2002). This object is the most peculiar among these four SOLE nebulae. This nebula does not show the hollow shell structure, but has a greater equatorial enhancement along the minor axis (P.A. of 149°). These peculiarities have been attributed to a higher degree of equatorial enhancement in the shell and to the inclination angle of the nebula that is marginally edge-on. However, our θ_{eq} measurement (101°), which is not consistent with this interpretation, appears affected by the bright starlight in this marginally optically thin nebula.

3.3. Discussion

3.3.1. Imaging-Polarimetric Characteristics of DUPLEX PPNs

Having reviewed the imaging-polarimetric characteristics of individual sources in §3.2, it now appears that the most prevalent characteristic among the observed DUPLEX PPNs is their point-symmetric appearance in the polarized surface brightness. This point-symmetric appearance of these nebulae in polarized light stems from the fact that one side of a lobe shows stronger polarization than the other and that the stronger polarization occurs at the opposite sides of the opposite lobes.

Among 13 DUPLEX PPNs in this compilation, 10 sources exhibit a sign of point-symmetry while the degree of point-symmetry varies among the sources. The exceptions are IRAS 09452, 10131, and 12419. In IRAS 10131 and 12419, the structure of the polarized surface brightness is not determined well since the polarized nebula is too compact in the former and the polarization flux is too weak in the latter. Thus, neglecting the two inconclusive cases, we have 10 out of 11 objects that display point-symmetric imaging-polarimetric characteristics. In IRAS 09452, the main lobe pair (the NE and S lobes in Fig. 2) is aligned along a straight line and so do the other lobes (the N and NW lobes) and there is no apparent indication of point-symmetric variation of polarization in the lobes. Thus, IRAS 09452 provides an example in which the imaging-polarimetric characteristics of the nebula are determined by the illumination effects. In fact, the N and NW lobes have been shown recently to be due to scattering of stray starlight leaking through fissures in the optically thick toroidal core of the CSE (Murakawa et al. 2005). None of these 10 DUPLEX PPNs that possess point-symmetry, however, shows obvious evidence for the illumination effects as does IRAS 09452.

In DUPLEX PPNs, the equatorial regions can be very optically thick in general as evidenced by the presence of a dust lane. Nevertheless, the bipolar lobes themselves are optically thin enough that they are seen via dust-scattered starlight. This allows us to adopt the same argument for SOLE PPNs that we used in Paper I and to investigate the structure of the lobes in DUPLEX PPNs by relating the I_p and P surface brightnesses to the amount of dust along the line of sight. Following a simple scattering angle effect (i.e., high degrees of polarization are expected from scattering at near 90° angles) as in Paper I, we can attribute the observed point-symmetric appearance in these 10 DUPLEX PPNs to the column density variations along the periphery of these nebulae. Since there is more dust on one side of a lobe than the other, we conclude that there is an azimuthal density gradient in these lobes. Asymmetric illumination can potentially induce similar point-symmetric nebula morphologies in polarized flux. However, polarized flux enhancements can occur anywhere and do not have to occur at the periphery of the nebulae. This is inconsistent with the observed trend in that the regions of enhanced polarization occurs near the periphery of the nebulae. Thus, we conclude that the asymmetric effect is less likely than the density effect as the cause for the point-symmetric appearance of the nebulae in polarized flux.

While the overall imaging-polarimetric morphology of the majority of the sample sources can be described as point-symmetric, there appear to be three distinct CSE structures among those point-symmetric nebulae. There are nebulae that show polarized fluxes near the periphery of the lobes in both I_p and P (IRAS 10178, 16594, 17150, 17423, and 19343). As discussed for SOLE PPNs in Paper I, this structure suggests that the lobes are hollow shells. Such hollow lobes can be created by either the cessation of mass loss in the polar directions or the sweeping up of the mass-loss ejecta into the polar directions. Recently, García-Arrendondo & Frank (2004) have shown hydro-dynamically that interactions between an AGB wind and a jet from an accretion disk can create a narrow-waist bipolar nebula if the jet dominates. A famous well-collimated bipolar PPN, M2-9 (e.g. Schwarz et al. 1997), which is very similar to IRAS 10178, has been interpreted as a symbiotic system evolving into a PN based on a scenario in which outflows emanate from the accretion disk (Livio & Soker 2001). In fact, IRAS 19343 has been recently suggested to be a symbiotic system based on a detailed spectroscopic study (Arrieta et al. 2005). Furthermore, the presence of precessing jets has been suggested in IRAS 17423 and 19343 based on the presence of shock excited knots (Bujarrabal et al. 1998b; Sánchez Contreras & Sahai 2001; Riera et al. 2003). Thus, such systems may reasonably explain the morphologies of these objects and even the oblique angle of the equatorial plane suspected in some of these objects (see below) may well be explained under the presence of precessing jets.

There are also nebulae that show P only near the periphery of the lobes but I_p inside the lobes (IRAS 10197, 17245, and 17441). These nebulae are also characterized by the very pronounced figure S shape. Unlike the previous case, the hollow P structure does not indicate the hollowness of the lobes since I_p is detected all over the lobes. The reduced P in the middle of the lobes is due to increased unpolarized light in the middle of the lobes. Since the central star is not very visible in these sources, it is not likely that the central star contributes to the increased presence of unpolarized light. Thus, we interpret that the unpolarized component of light is increased

in the middle of these nebulae due to multiple scattering in their optically thicker equatorial regions. Such enhanced optical depths in the vicinity of the central star along the equatorial plane can be attributed, for example, to the presence of a disk around the central star. It has been shown recently that a warped equatorial density enhancement can generate point-symmetric lobes by a two-fluid hydro-dynamical simulations (Icke 2003; Rijkhorst et al. 2004). Similarities between models and the nebula structure (especially of IRAS 10197) are remarkable.

There are yet another nebulae that display clumpiness in the polarized surface brightness distribution (IRAS 04395 and AFGL 2688). As previously noted, the clumpy structure of IRAS 04395 may be due to episodic mass loss or instabilities in the outflows. The bipolar lobes of AFGL 2688 also show signs of hollowness but their I_p structure (especially of the northern lobe) is clumpy, and therefore, AFGL 2688 may belong to the previous group. However, none of the sources in the previous group shows the presence of the concentric arcs as in AFGL 2688. Thus, AFGL 2688 may be a very unique object. Although the nebula structure is inconclusive due to its compactness, IRAS 10131 may be related to AFGL 2688 because IRAS 10131 also shows some arcs in the CSE (Schmidt et al. 2002).

3.3.2. SOLE and DUPLEX Morphologies

In this section we compare the morphological characteristics of SOLE and DUPLEX PPNs in this the most complete compendium of imaging-polarimetric data for PPNs taken with *HST* including data presented in Paper I. In Paper I, we have shown that (1) optically thin SOLE PPNs consist of a hollow spheroidal shell with a built-in equatorial density enhancement, which manifests itself as the toroidal structure and (2) there is a range of optical depths, which can influence the observed morphological traits even among SOLE CSEs. In the present work, we have concluded that there exist the azimuthal density gradient in addition to equatorial density enhancements in the bipolar lobes of optically thicker DUPLEX PPNs.

The distinction between SOLE and DUPLEX PPNs was initially proposed based primarily on the presence/absence of the optically thick dust lane (Ueta et al. 2000). The present imaging polarimetry provides an alternative means to differentiate these two morphological types. As we have reviewed in § 3.3.1, we have found a prevalent morphological feature - point-symmetry in the surface brightness distribution of polarized flux. This point-symmetric appearance is probably due to the azimuthal density gradient being reversed in the opposing lobes above and below the equatorial plane. On the other hand, in SOLE PPNs there is no reversal of the azimuthal density gradient above and below the equatorial plane, although the azimuthal density gradient is present. The best example for this is IRAS 07134 presented in Paper I, in which the presence of the azimuthal density gradient has been shown in the dust and CO gas distribution in its shell (Meixner et al. 2004).

Thus, it appears that mechanisms that generate a reversal in the azimuthal density gradient in the opposite lobes are related to the fundamental nature of the DUPLEX nebulae while these mechanisms do not operate in the SOLE nebulae. Therefore, we postulate that the emergence of the reversal in the azimuthal dust density distribution is directly linked to the origin of the morphological bifurcation between SOLE and DUPLEX PPNs. However, it is still inconclusive at this point what causes this reversal.

3.3.3. Oblique Orientation of the Equatorial Plane

In the present work, we have adopted θ_{eq} , the integrated θ over an aperture, as a measure of the orientation of the equatorial plane (modulo 90° to be precise). In conventional imaging, the orientation of the equatorial plane is inferred from the appearance of the dust lane and/or of the bipolar lobes. As we have noted earlier, the way starlight gets scattered in the equatorial regions can be strongly influenced by the local density enhancements. Therefore, the silhouette morphology of dust lanes, especially in high spatial resolution imaging data, can be susceptible to the local density distribution. In such cases, imaging polarimetry can alternatively constrain the orientation of the equatorial plane better than the conventional imaging.

We have seen in §3.3.2 that θ_{eq} does not necessarily correspond to the orientation of the apparent dust lane seen in the I data. Among 13 DUPLEX PPNs, we have found in 10 sources that the discrepancy between θ_{eq} and the orientation of the bipolar axis is more than the quoted error, assuming that the uncertainty in the bipolar axis orientation is $\sim 2^\circ$. The two angles are equal within errors in one case (IRAS 17150). In two cases θ_{eq} is not reliably fixed probably due to the bright central star and faint polarized surface brightnesses (IRAS 12419 and 16594). In the 10 oblique cases, however, the determination of the orientation of the bipolar axis from the I_p structure is somewhat subjective: the 2° uncertainty may be inappropriate for three cases (IRAS 17245, IRAS 17423, and AFGL 2688). Even so, there are still seven sources in which the equatorial plane is more than $\sim 10^\circ$ oblique from the perpendicular orientation with respect to the bipolar axis, and there are more than twice as many oblique cases as orthogonal cases.

Even if we take a stricter stance on the subjectivity in defining the bipolar axis and on our informal error analysis in deriving θ_{eq} , there are cases in which the oblique angle is more than 20° (IRAS 17441 and 19343). This issue needs to be investigated further in future as it may be related to the mechanisms to generate the equatorial density enhancement and bipolar lobes.

4. SUMMARY

We have presented a compendium of near-IR imaging-polarimetric data of evolved star CSEs that have been obtained with *HST*/NICMOS to date, in order to study polarization characteristics of these CSEs, especially of optically thicker bipolar DUPLEX PPNs. The data have shown that their point-symmetric appearance is prevalent (seen in 10 out of 11 objects). Since the prevalent point-symmetry does not seem to be due to the illumination effects in almost all cases (except for one), we have concluded that the observed point-symmetry is due to the presence of the azimuthal density gradient in the CSEs.

These point-symmetric nebulae can be grouped into three based on the detailed morphologies. The first group consists of objects that show polarized fluxes near the periphery of the lobes in both I_p and P (IRAS 10178, 16594, 17150, 17423, and 19343). By using the same argument as in Paper I, we suggest that the bipolar lobes in these sources are hollow shells. The second group consists of objects that are characterized by the very pronounced figure S shape and show P only near the periphery of the lobes but I_p inside the lobes (IRAS 10197, 17245, and 17441). Since the reduced P in the middle of the nebula is due to the increased unpolarized light in the nebula, we interpret that multiple scattering takes place in the relatively dense equatorial regions in these sources. The last group is characterized by their clumpy nebulae (IRAS 04395 and AFGL 2688) that may be due to episodic mass loss or instabilities in the outflows. While the lobes of AFGL 2688 show similarities to the second group, the presence of the concentric arcs makes it rather unique. IRAS 10131 may be related to AFGL 2688 because of the presence of arcs.

We have found that the ways in which the azimuthal density gradient is manifested in SOLE and DUPLEX PPNs are very distinct: the direction of the azimuthal density gradient in DUPLEX PPNs is reversed in the opposing lobes above and below the equatorial plane whereas such a reversal is not seen in SOLE PPNs. The most probable explanation for this seems to be the presence of precessing outflows into the opposite directions and/or magnetic field that is reversed its polarity above and below the equatorial plane. We have also found indications that the equatorial plane of the system (defined by θ_{eq}) is not necessarily orthogonal to the axis of the apparent bipolar structure in the total intensity data (at least 7 out of 10 sources). There are cases in which the oblique angle is more than 20° (IRAS 17441 and 19343). Therefore, we have concluded that the occurrence of the oblique orientation of the equatorial plane with respect to the bipolar axis is real and that this issue needs to be investigated further in future.

This research is based on observations with the NASA/ESA Hubble Space Telescope, obtained at the Space Telescope Science Institute (STScI), which is operated by the Association of Universities for Research in Astronomy, Inc. (AURA) under NASA contract No. NAS 5-26555. Authors acknowledge financial support by NASA STI 9377.05-A. Ueta also acknowledge partial support from the project IAP P5/36 financed by Federal Services for Scientific, Technical and Cultural Affairs of the Belgian State and the Universities Space Research Association SOFIA (Stratospheric Observatory for Infrared Astronomy) office at NASA Ames Research Center as well as a US National Research Council Research Associateship Award and a NASA Postdoctoral Program Award.

REFERENCES

- Allen, D. A., Hyland, A. R., & Caswell, J. L. 1980, *MNRAS*, 192, 505
 Arrieta, A., Torres-Peimbert, S., & Georgiev, L. 2005, *ApJ*, 623, 252
 Balick, B., & Frank, A. 2002, *ARA&A*, 40, 439
 Batcheldor, D., Robinson, A., Axon, D., Hines, D. C., Sparks, W., & Tadhunter, C. 2006, *PASP*, 118, 642
 Becklin, E. E., Frogel, J. A., Hyland, A. R., Kristian, J., & Neugebauer, G. 1969, *ApJ*, 158, L133
 Bujarrabal, V., Alcolea, J., & Neri, R. 1998, *ApJ*, 504, 915
 Bujarrabal, V., Alcolea, J., Neri, R., & Grewing, M. 1994, *ApJ*, 436, L169
 Bujarrabal, V., Alcolea, J., Sahai, R., Zamorano, J., & Zijlstra, A. 1998, *A&A*, 331, 361
 Bujarrabal, V., Gómez-González, J., Bachiller, R., & Martín-Pintado, J. 1988, *A&A*, 204, 242
 Calvet, N., & Cohen, M. 1978, *MNRAS*, 182, 687
 Capps, R. W., & Dyck, H. M. 1972, *ApJ*, 175, 693
 Capps, R. W., & Knacke, R. F. 1976, *PASP*, 88, 224
 Cohen, M. 1979, *MNRAS*, 186, 837
 Cox, P., Maillard, J.-P., Huggins, P. J., Forveille, T., Simons, D., Guilletoleau, S., Rigaut, F., Bachiller, R., & Omont, A. 1997, *A&A*, 321, 907
 Dayal, A., Hoffmann, W. F., Biegling, J. H., Hora, J. L., Deutsch, L. K., & Fazio, G. G. 1998, *ApJ*, 492, 603
 Dickinson, M., et al. 2002, in "HST NICMOS Data Handbook Version 5.0", ed. B. Mobasher (Baltimore: STScI)

- Dyck, H. M., Forbes, F. F., & Shawl, S. J. 1971, *AJ*, 76, 901
- García-Arrendondo, F. & Frank, A. 2004, *ApJ*, 600, 992
- García-Hernández D. A., Manchado, A., García-Lario, P., Benítez Cañete, A., Acosta-Pulido, J. A., Pérez García, A. M. 2004, in *ASP Conf. Ser. Vol. 313, Asymmetric Planetary Nebulae III*, eds. M. Meixner, J. Kastner, B. Balick, & N. Soker (San Francisco: ASP), 367
- García-Lario, P., Riera, A., & Manchado, A. 1999, *ApJ*, 526, 854
- García-Segura, G., López, A., & Franco, J. 2005, *ApJ*, 618, 919
- Gledhill, T. M. 2005, *MNRAS*, 356, 883
- Gledhill, T. M., Chrysostomou, A., Hough, J. H., & Yates, J. A. 2001, *MNRAS*, 322, 321
- Goto, M., Kobayashi, N., Terada, H., & Tokunaga, A. 2002, *ApJ*, 572, 276
- Habing, H. J., & Blommaert, J. A. D. L. 1993, in *Planetary nebulae, IAU Symp. 155*, eds. R. Weinberger & A. Acker, 243
- Hines, D. C., Schmidt, G. D., & Schneider, G. 2000, *PASP*, 112, 983
- Hrivnak, B. J. 1995, *ApJ*, 438, 341
- Hrivnak, B. J., Kwok, S., & Volk, K. 1989, *ApJ*, 346, 265
- Hrivnak, B. J., Kelly, D. M., & Su, K. Y. L. 2004, in *ASP Conf. Ser. Vol. 313, Asymmetric Planetary Nebulae III*, eds. M. Meixner, J. Kastner, B. Balick, & N. Soker (San Francisco: ASP), 175
- Hrivnak, B. J., & Kwok, S. 1999, *ApJ*, 513, 869
- Hrivnak, B. J., Kwok, S., Su, K. Y. L. 1999, *ApJ*, 524, 849
- Hrivnak, B. J., Reddy, B. E. 2003, *ApJ*, 590, 1049
- Iben, I. Jr., & Renzini, A. 1983, *ARA&A*, 21, 271
- Icke, V. 2003, *A&A*, 405, L11
- Johnson, J. J., & Jones, T. J. 1991, *AJ*, 101, 1735
- Jura, M., Chen, C., & Werner, M. W. 2000a, *ApJ*, 544, L141
- Kastner, J. H., Weintraub, D. A., Gatley, I., & Henn, L. 2001, *ApJ*, 546, 279
- Koekemoer, A. M., et al. 2002, "HST Dither Handbook", Version 2.0 (Baltimore: STScI)
- Kruszewski, A. 1971, *AJ*, 76, 576
- Kruszewski, A., & Coyne, G. V. 1976, *AJ*, 81, 641
- Kwok, S. 1993, *ARA&A*, 31, 63
- Kwok, S., Su, K. Y. L., Hrivnak, B. J. 1998, *ApJ*, 501, L117
- Kwok, S., Volk, K., & Hrivnak, B. J. 2002, *ApJ*, 573, 720
- Livio, M., & Soker, N. 2001, *ApJ*, 552, 685
- Mauron, N., & Huggins, P. J. 2000, *A&A*, 359, 707
- Meixner, M., Skinner, C. J., Graham, J. R., Keto, E., Jerrigen, J. G., & Arens, J. F. 1997, *ApJ*, 482, 897
- Meixner, M., Ueta, T., Dayal, A., Hora, J. L., Fazio, G., Hrivnak, B. J., Skinner, C. J., Hoffmann, W. F., & Deutsch, L. K. 1999, *ApJS*, 122, 221
- Meixner, M., Ueta, T., Bobrowsky, M., & Speck, A. K. 2002, *ApJ*, 571, 936
- Meixner, M., Zalucha, A., Ueta, T., Fong, D., & Justtanont, K. 2004, *ApJ*, 614, 371
- Murakawa, K., Suto, H., Oya, S., Yates, J. A., Ueta, T., & Meixner, M. 2005, *A&A*, 436, 601
- Ney, E. P., Merrill, K. M., Becklin, E. E., Neugebauer, G., & Wynn-Williams, C. G. 1975, *ApJ*, 198, L129
- Oppenheimer, B. D., Biegging, J. H., Schmidt, G. D., Gordon, K. D., Misselt, K. A., & Smith, P. S. 2005, *ApJ*, 624, 957
- Osterbart, R., Balega, Y. Y., Blöcker, T., Men'shchikov, A. B., & Weigelt, G. 2000, *A&A*, 357, 169
- Renzini, A. 1981, in *Physical Processes in Red Giants*, eds. I. Iben Jr. & A. Renzini (Dordrecht: Reidel), 431
- Riera, A., García-Lario, P., Manchado, A., Bobrowsky, M., & Estalella, R. 2003, *A&A*, 401, 1039
- Rijkhorst, E. J., Icke, V., & Mellema, G. 2004, in *ASP Conf. Ser. Vol. 313, Asymmetric Planetary Nebulae III*, eds. M. Meixner, J. Kastner, B. Balick, & N. Soker (San Francisco: ASP), 472
- Sahai, R. 1999, *ApJ*, 524, L125
- Sahai, R., Bujarrabal, V., & Zijlstra, A. 1999, *ApJ*, 518, L115
- Sahai, R., Hines, D. C., Kastner, J. H., Weintraub, D. A., Trauger, J. T., Rieke, M. J., Thompson, R. I., & Schneider, G. 1998, *ApJ*, 492, L163
- Sahai, R., & Sánchez Contreras, C. 2004, in *ASP Conf. Ser. Vol. 313, Asymmetric Planetary Nebulae III*, eds. M. Meixner, J. Kastner, B. Balick, & N. Soker (San Francisco: ASP), 32
- Sahai, R., Zijlstra, A., Bujarrabal, V., & te Lintel Hekkert, P. 1999, *AJ*, 117, 1408
- Sánchez Contreras, C., & Sahai, R. 2001, *ApJ*, 553, L173
- Scarrott, S. M., & Scarrott, R. M. J. 1995, *MNRAS*, 277, 277
- Schmidt, G. D., Angel, J. R., & Beaver, E. A. 1978, *ApJ*, 219, 477
- Schmidt, G. D., Hines, D. C., & Swift, S. 2002, *ApJ*, 576, 429
- Schwarz, H., Aspin, C., Corradi, R. L. M., & Reipurth, B. 1997, *A&A*, 319, 267
- Serkowski, K., & Shawl, S. J. 2001, *AJ*, 122, 2017
- Sevenster, M. N. 2002, *AJ*, 123, 2772
- Shawl, S. J., & Zellner, B. 1970, *ApJ*, 162, L19
- Skinner, C. J., Meixner, M., & Bobrowsky, M. 1998, *MNRAS*, 300, L29
- Su, K. Y. L., Hrivnak, B. J., Kwok, S., & Sahai, R. 2003, *AJ*, 126, 848
- Su, K. Y. L., Volk, K., Kwok, S., & Hrivnak, B. J. 1998, *ApJ*, 508, 744
- Taylor, K. N. R., & Scarrott, S. M. 1980, *MNRAS*, 193, 321
- Trammell, S. R., & Goodrich, R. W. 1996, *ApJ*, 468, L107
- Trammell, S. R., & Goodrich, R. W. 2002, *ApJ*, 579, 688
- Trammell, S. R., Dinerstein, H. L., & Goodrich, R. W. 1994, *AJ*, 108, 984
- Tuthill, P. G., Monnier, J. D., Danchi, W. C., & Lopez, B. 2000, *ApJ*, 543, 284
- Ueta, T., Meixner, M., & Bobrowsky, M. 2000, *ApJ*, 528, 861
- Ueta, T., Fong, D., & Meixner, M. 2001a, *ApJ*, 557, L117
- Ueta, T., Meixner, M., Hinz, P. M., Hoffmann, W. F., Brandner, W., Dayal, A., Deutsch, L. K., Fazio, G. G., & Hora, J. L. 2001b, *ApJ*, 557, 831
- Ueta, T., Murakawa, K., & Meixner, M. 2005, *AJ*, 129, 1625 (Part I)
- Ueta, T., Murakawa, K., & Meixner, M. 2006, *ApJ*, 641, 1113
- Ulrich, B. T., Neugebauer, G., McCammon, D., Leighton, R. B., Hughes, E. E., & Becklin, E. 1966, *ApJ*, 146, 288
- Van de Steene, G. C., & van Hoof, P. A. M. 2003, *A&A*, 406, 773
- Van Winckel, H. 2003, *ARA&A*, 41, 391
- Weigelt, G., Balega, Y. Y., Blöcker, T., Hofmann, K.-H., Men'shchikov, A. B., & Winters, J. M. 2002, *A&A*, 392, 131
- Wegner, G., & Glass, I. S. 1979, *MNRAS*, 188, 327
- Weintraub, D. A., Kastner, J. H., Hines, D. C., & Sahai, R. 2000, *ApJ*, 531, 401
- Westbrook, W. E., Willner, S. P., Merrill, K. M., Schmidt, M., Becklin, E. E., Neugebauer, G., & Wynn-Williams, C. G. 1975, *ApJ*, 202, 407
- Whitney, B. A., & Hartmann, L. 1993, *ApJ*, 402, 605

TABLE 1
HST/NICMOS IMAGING-POLARIMETRIC OBSERVATIONS OF EVOLVED STARS

Source	Alternative Names	Date	FILTER ^a	SAMP_SEQ	NSAMP	DITHER		EXPTIME ^b (sec)	ORIENTAT ^c (deg)	PID	Reference
						PATTERN	NPTS				
Source Data											
IRAS 02168–0312	Mira, O Cet	1998 Aug 11	POL-S	STEP8	13	NONE	...	135.8608	34.7588	7416	
		1998 Aug 11	POL-L	STEP32	4	TWO-CHOP	4	169.8279	33.9539	7416	
IRAS (z)02229+6208 ^d		2003 Mar 28	POL-S	STEP8	16	SPIRAL	4	319.6832	169.035	9377	1
IRAS 04296+3429		2003 Mar 28	POL-S	STEP8	19	SPIRAL	5	519.5079	-149.313	9377	1, 2
IRAS 04395+3601	AFGL/CRL 618	2003 Nov 26	POL-L	SPARS64	13	SPIRAL	4	2559.868	-35.4301	9430	
IRAS 06530–0213		2003 Mar 29	POL-S	STEP8	19	SPIRAL	5	519.5079	-131.793	9377	1, 2
IRAS 07134+1005	HD 56126	2003 Mar 29	POL-S	STEP8	19	SPIRAL	5	519.5079	-129.432	9377	1
IRAS 09452+1330	IRC +10 216, CW Leo	1997 Apr 30	POL-S	STEP8	9	NONE	...	71.89689	-113.462	7120	3, 4
IRAS 10131+3049	CIT 6, RW LMi	1998 May 5	POL-S	STEP16	12	SPIRAL	4	319.7775	-109.901	7854	5
		1998 Oct 11	POL-S	STEP16	11	SPIRAL	4	255.8052	80.8889	7854	5
		1998 Feb 23	POL-L	MCAMRR	12	SPIRAL	4	3.32561	-52.5125	7854	5
		1998 May 5	POL-L	MCAMRR	12	SPIRAL	4	3.32561	-110.707	7854	5
		1998 Oct 11	POL-L	MCAMRR	11	SPIRAL	4	3.02328	80.0841	7854	5
		1998 Mar 6	POL-L	STEP32	17	SPIRAL	3	863.8767	124.507	7840	
		1998 May 18	POL-L	STEP32	12	SPIRAL	3	383.8884	-133.434	7840	
IRAS 10178–5958	Hen 3-404, Roberts 22	1998 May 18	POL-L	STEP32	12	SPIRAL	3	383.8884	-133.434	7840	
IRAS 10197–5750	Boomerang Nebula	1998 Sep 12	POL-L	STEP32	17	SPIRAL	3	863.8767	-65.4931	7840	
IRAS 12419–5414		1998 May 2	POL-L	STEP32	17	SPIRAL	3	863.8767	78.9531	7840	1, 6
IRAS 16594–4656		1998 Aug 16	POL-L	STEP64	16	SPIRAL	3	1343.842	-150.493	7840	6
IRAS 17150–3224		1998 Aug 16	POL-L	STEP64	16	SPIRAL	3	1343.842	-150.493	7840	6
IRAS 17245–3951	OH 348.81–2.84	1998 Apr 30	POL-L	STEP16	24	SPIRAL	3	815.5839	64.7606	7840	6, 7
IRAS 17423–1755	Hen 3-1475	1997 Aug 9	POL-S	STEP8	21	SPIRAL	2	239.7774	-137.381	7285	
IRAS 17441–2411		1998 Mar 10	POL-L	STEP32	21	SPIRAL	3	1247.867	45.665	7840	6
IRAS 19343+2926	M 1-92	1998 Apr 24	POL-L	STEP128	12	XSTRIP	3	767.8638	29.2312	7839	
AFGL 2688	Egg Nebula, V1610 Cyg	1998 Apr 8	POL-S	STEP16	20	SPIRAL	4	831.556	58.3121	7423	3
		2002 Oct 6	POL-S	STEP16	20	SPIRAL	4	831.556	-117.002	9644	
		1997 Apr 8	POL-L	STEP16	26	SPIRAL	4	1215.39	56.3451	7115	8, 9
		2002 Oct 6	POL-L	STEP16	26	SPIRAL	4	1215.39	-117.752	9644	
PSF Calibration Source Data											
HD 12088		2003 Mar 28	POL-S	STEP1	19	SPIRAL	5	79.7868	162.51	9377	1
BD +32° 3739		1997 Sep 1	POL-S	SCAMRR	9	NONE	...	11.368	-92.7652	7692	1, 3
		2002 Sep 9	POL-S	SCAMRR	9	SPIRAL	4	12.992	-108.88	9644	1
		1997 Sep 1	POL-L	STEP1	9	NONE	...	41.86784	-93.5733	7692	1, 3
		2003 Jun 8	POL-L	STEP1	9	SPIRAL	4	47.84896	-109.63	9644	1

REFERENCES. — 1. Ueta et al. (2005), 2. Gledhill (2005), 3. Hines et al. (2000), 4. Osterbart et al. (2000), 5. Schmidt et al. (2002), 6. Su et al. (2003), 7. Gledhill et al. (2001), 8. Sahai et al. (1998), 9. Weintraub et al. (2000)

^a POL-S: short wavelength polarizers (0.8–1.3 μ m, centered at 1.1 μ m); POL-L: long wavelength polarizers (1.89–2.1 μ m, centered at 2.05 μ m).

^b Total exposure time per polarizer.

^c The ORIENTAT header parameter refers to PA of the image +y axis (degrees E of N).

^d The “z” prefix in the IRAS designation is given to indicate the fact that this object was found in the Faint Source Reject File in the IRAS Faint Source Survey (Hrivnak et al. 1999).

TABLE 2
SUMMARY OF *HST*/NICMOS IMAGING POLARIMETRY OF THE CIRCUMSTELLAR SHELL AROUND EVOLVED STARS

Source	Measured Coordinates (J2000) ^a			Band ^b	Flux				Polarized Surface Brightness Distribution		
	R.A.	Decl.	Offset (arcsec)		I (mJy)	I_p (mJy)	P_{\max}^c (%)	$\langle P \rangle^c$ (%)	Morphology ^d	Size (arcsec)	P.A. ^e (deg)
IRAS 02229	02 26 41.79	+62 21 22.2	0.12 ± 0.31	POL-S	4800	1200	60	34 ± 11	ELS	2.1 × 1.3	59
IRAS 04296	04 32 56.95	+34 36 13.1	0.06 ± 0.17	POL-S	340	60	84	29 ± 13	Dual ELS (hollow)	2.1 × 0.7	26
IRAS 04395	04 42 53.61	+36 06 53.8	0.23 ± 0.16	POL-L	275	38	54	19 ± 10	BPL (inverse S)	15.0 × 3.4	94
IRAS 06530	06 55 31.80	-02 17 28.3	0.04 ± 0.20	POL-S	380	67	68	33 ± 14	ELS + Cusp (hollow)	2.7 × 1.0	20
IRAS 07134	07 16 10.27	+09 59 48.5	0.08 ± 0.27	POL-S	9300 ^f	2000	81	44 ± 20	ELS (hollow)	4.8 × 4.0	25
IRAS 09452	09 47 57.37	+13 16 42.8	0.04 ± 0.13	POL-S	4590	808	65	28 ± 12	Fragmented BPL	5.4 × 2.2	22
IRAS 10131 (1998-05-05)	10 16 02.26	+30 34 18.8	0.06 ± 0.09	POL-S	2360	465	60	26 ± 14	BPS	10.0 × 3.6	35
(1998-10-11)	10 16 02.19	+30 34 18.6	0.08 ± 0.16	POL-S	8470	1540	60	25 ± 13			35
IRAS 10178	10 19 32.48	-60 13 28.8	0.09 ± 0.07	POL-L	554	146	56	27 ± 12	BPL (S)	16.4 × 2.6	73
IRAS 10197	10 21 33.88	-58 05 47.7	0.26 ± 0.11	POL-L	1320	330	65	29 ± 14	BPS (S) + Protrusions	7.6 × 5.6	23
IRAS 12419	12 44 46.07	-54 31 13.5	0.06 ± 0.25	POL-L	380	35	41	12 ± 8	BPS (X)	10.0 × 7.0	163
IRAS 16594	17 03 10.04	-47 00 27.0	0.06 ± 0.14	POL-L	620	66	73	39 ± 16	ELS + Cusp	5.0 × 2.2	82
IRAS 17150	17 18 19.81	-32 27 21.2	0.14 ± 0.07	POL-L	230	60	70	26 ± 18	BPL (S)	6.6 × 2.2	122
IRAS 17245	17 28 04.58	-39 53 45.1	0.24 ± 0.08	POL-L	145	18	48	17 ± 11	BPL	2.0 × 1.3	15
IRAS 17423	17 45 14.23	-17 56 47.0	0.15 ± 0.11	POL-S	272 ^g	48 ^g	51	26 ± 12	BPL (S) + Knots	10.9 ^g × 1.7	133
IRAS 17441	17 47 13.51	-24 12 52.0	0.19 ± 0.16	POL-L	212	57	59	16 ± 14	BPL (S)	4.0 × 2.1	1
IRAS 19343	19 36 19.02	+29 32 50.2	0.27 ± 0.22	POL-L	3360	373	52	22 ± 13	BPL (S)	12.9 × 3.9	131
AFGL 2688 (1998-04-08)	21 02 18.66	+36 41 37.4	0.17 ^h	POL-S	413 ^g	226 ^g	89	50 ± 18	BPL (inverse S)	15.0 ^g × 4.0	12
(2002-10-06)	21 02 18.53	+36 41 36.2	0.23 ^h	POL-S	469 ^g	272 ^g	81	51 ± 15			
(1997-04-08)	21 02 18.76	+36 41 36.9	0.29 ^h	POL-L	599 ^g	284 ^g	74	23 ± 17	BPL (inverse S)	23.7 ^g × 3.7	12
(2002-10-06)	21 02 18.55	+36 41 36.0	0.22 ^h	POL-L	637 ^g	295 ^g	73	23 ± 16			

^a Of the centrosymmetric polarization pattern center. Offset is the angular distance from the pattern center to the I peak with an associated error in the pattern center determination.

^b POL-S: short wavelength polarizers (0.8–1.3 μm , centered at 1.1 μm); POL-L: long wavelength polarizers (1.89–2.1 μm , centered at 2.05 μm).

^c P_{\max} is the maximum polarization strength detected, while $\langle P \rangle$ refers the mean P and its standard deviation.

^d ELS: elliptical shell; BPS: bipolar shell without any apparent dust lane; BPL: bipolar lobes separated by a dust lane.

^e Of the nebula (counter-clockwise east of north).

^f The measured flux value is three times higher than the previously observed value (see §4 in Paper I).

^g The observed field did not cover the entire nebula.

^h No I peak.

TABLE 3
SUMMARY OF APERTURE POLARIMETRY

Source	Band	Aperture (arcsec)	P^a (%)	θ_{eq}^a (deg)	P.A. ^b (deg)
IRAS 02229	POL-S	0.4	6.1 ± 1.0	101 ± 1	59
IRAS 04296	POL-S	0.6	5.7 ± 1.0	11 ± 1	26, 99
IRAS 04395	POL-L	1.2	7.7 ± 0.5	83 ± 1	94
IRAS 06530	POL-S	1.6	2.7 ± 1.5	159 ± 2	20
IRAS 07134	POL-S	0.6	4.9 ± 2.0	136 ± 1	25
IRAS 09452	POL-S	0.8	11.2 ± 1.0	32 ± 1	22
IRAS 10131 (1998-05-05)	POL-S	0.6	4.6 ± 0.7	49 ± 1	35
(1998-10-11)	POL-S	0.6	5.4 ± 0.7	43 ± 1	35
IRAS 10178	POL-L	1.0	3.0 ± 1.5	80 ± 1	73
IRAS 10197	POL-L	3.0	8.5 ± 1.0	34^c	23
IRAS 12419	POL-L	0.9	3.5 ± 1.0	57^c	163
IRAS 16594	POL-L	0.9	0.7 ± 0.2	22 ± 6	82
IRAS 17150	POL-L	2.4	17.5 ± 2.0	120 ± 1	122
IRAS 17245	POL-L	1.1	7.1 ± 0.3	21^c	15
IRAS 17423	POL-S	2.2	5.2 ± 0.1	128 ± 2	133
IRAS 17441	POL-L	1.0	11.7 ± 1.0	28 ± 4	1
IRAS 19343	POL-L	0.9	2.3 ± 4.0	151^c	131
AFGL 2688 (1997-04-08)	POL-L	3.8	42.5 ± 1.0	19 ± 1	12
(2002-10-06)	POL-L	3.0	37.3 ± 0.8	17 ± 1	12

^a These errors are not via a formal error analysis. See text for details.

^b Of the nebula (counter-clockwise east of north). Typically $\pm 2^\circ$ error. Reproduced from Table 2.

^c Error less than 0.5 deg.

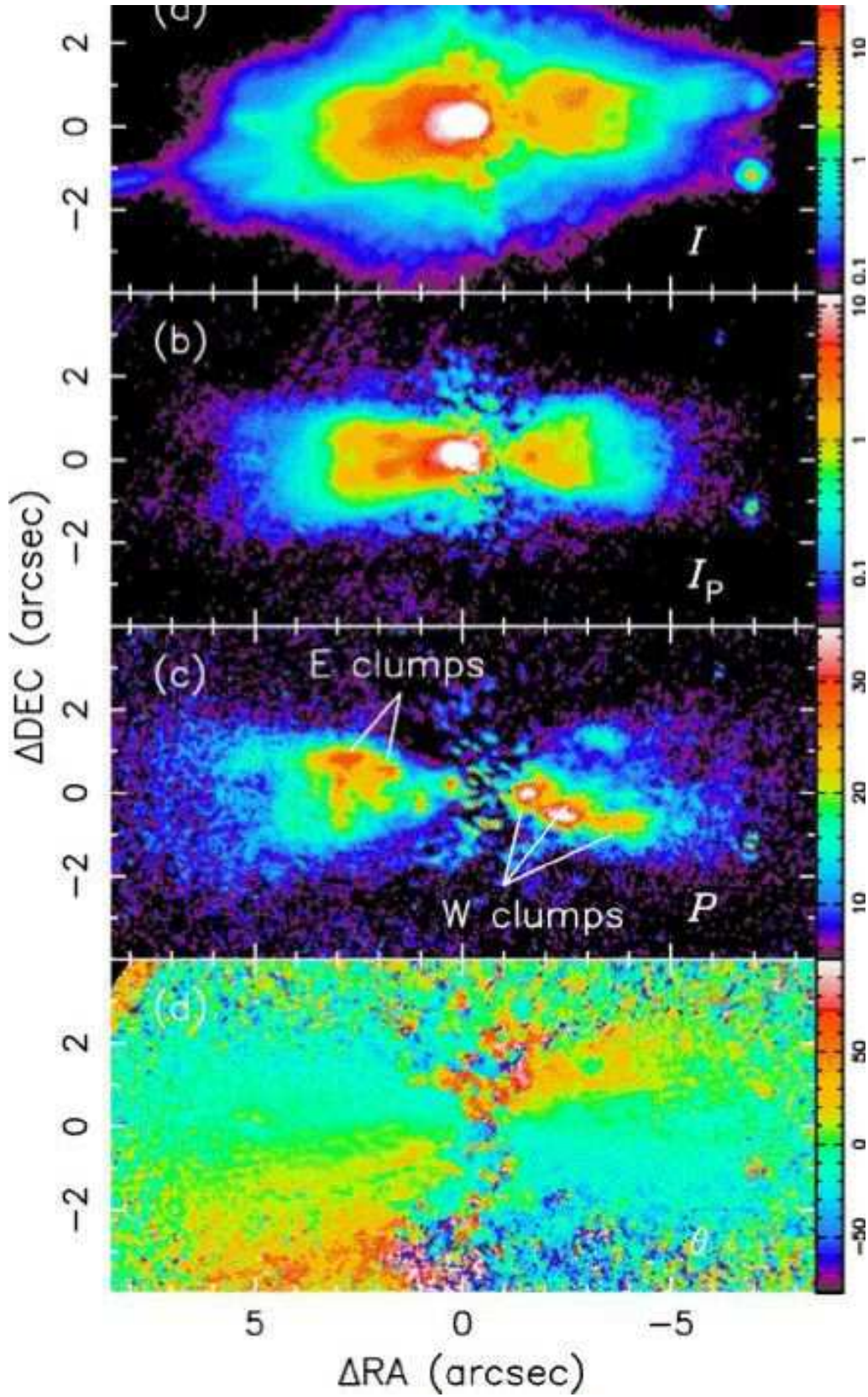


FIG. 1.— Imaging polarimetric maps of IRAS 04395+3601 in the (a) total intensity, I , (b) polarized intensity, I_p , (c) polarization strength, P , and (d) polarization P.A., θ . The maps are in the standard orientation (north is up, east to the left) and centered at the θ center with tickmarks showing the right ascension and declination offsets in arcseconds. The wedges indicate the scale of the image tone in data number per second (DN s^{-1} , which is to be multiplied by PHOTOFNU [see Table 2 in Paper I] to convert to Jy) for I and I_p , in percent for P , and degrees east of north in θ (i.e. P.A. 0° means the polarization vector, which is perpendicular to the scattering plane, is oriented in the north-south direction). The east and west clumps are indicated.

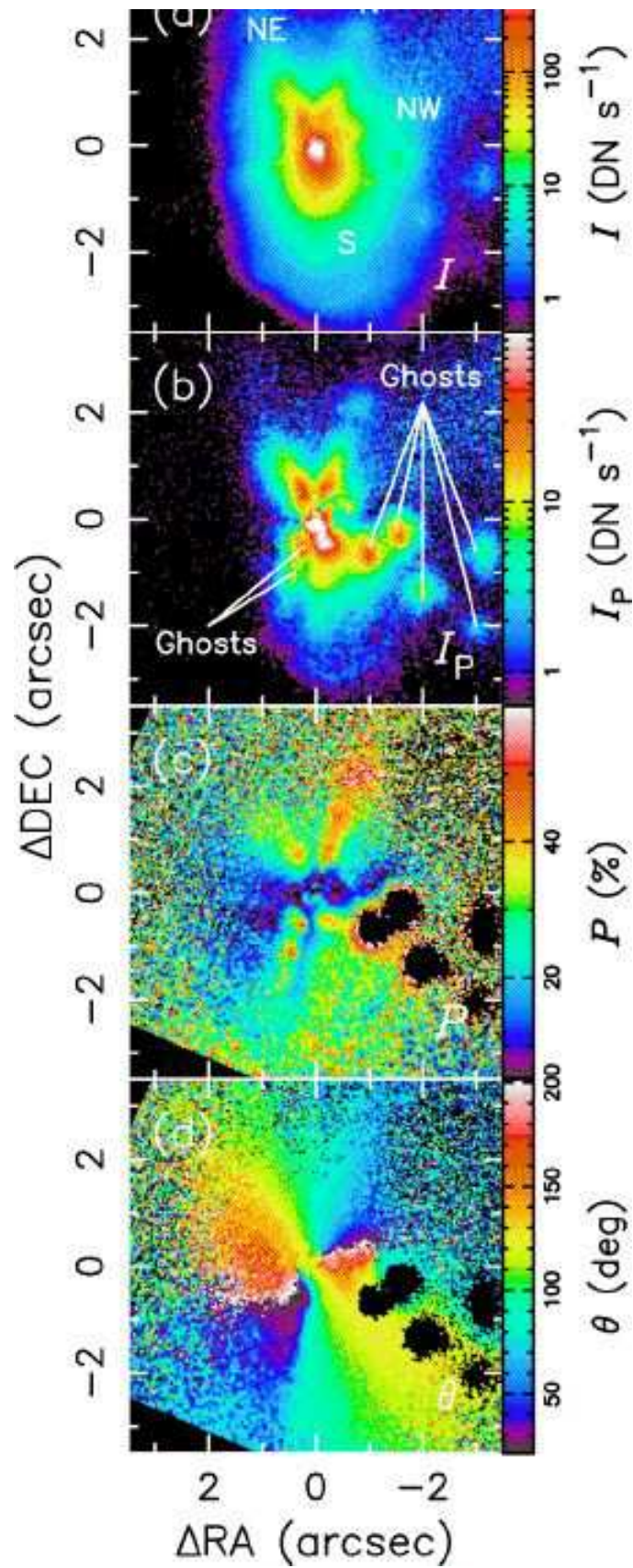


FIG. 2.— Same as Fig. 1, but for IRAS 09452+1330. Each lobe is identified with its designation, NE, N, NW, SE, and SW.

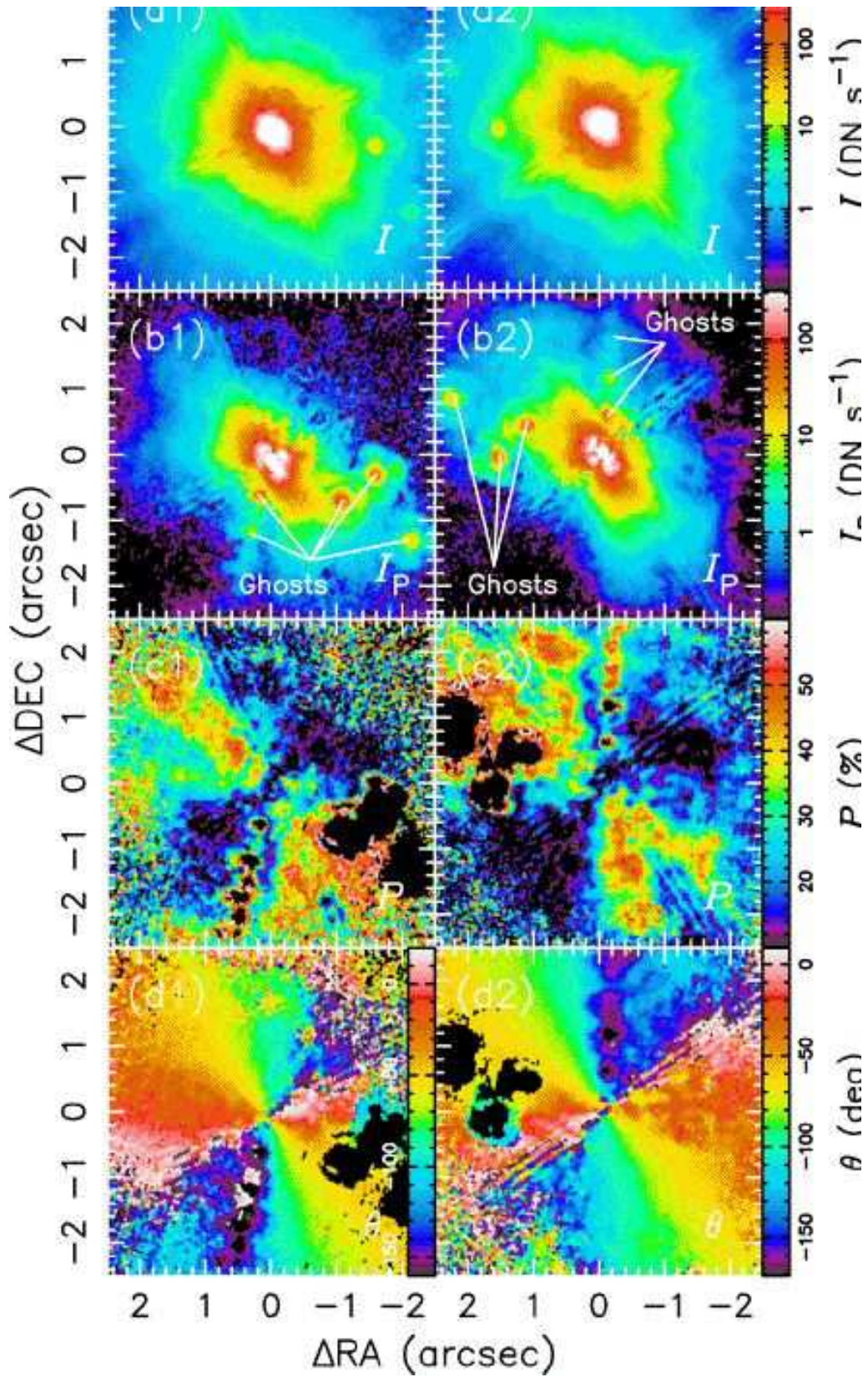


FIG. 3.— Same as Fig. 1, but for the two-epoch observations of IRAS 10131+3049 (Left: 1998 May 5, Right: 1998 Oct 11). The polarization ghosts are indicated.

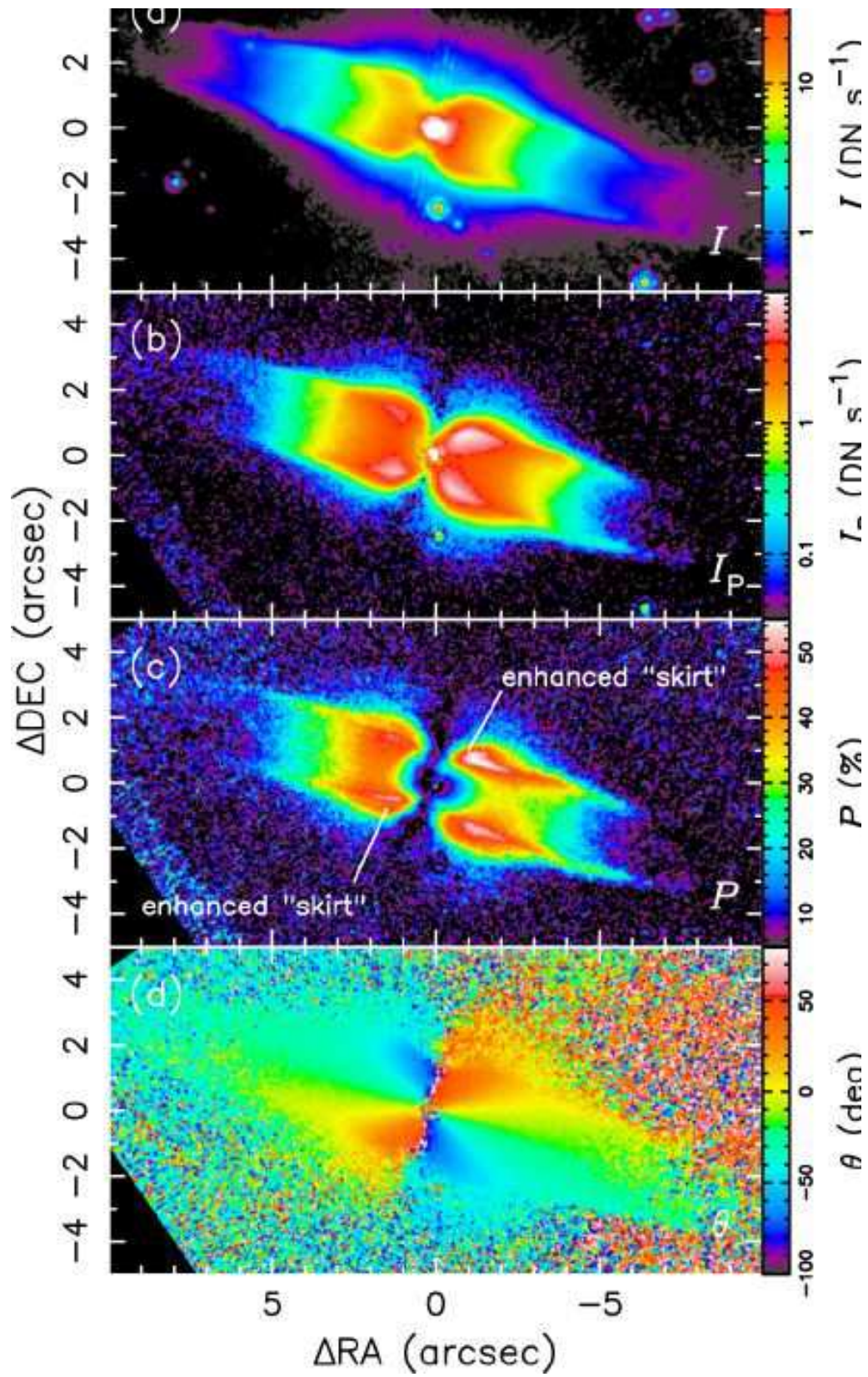


FIG. 4.— Same as Fig. 1, but for IRAS 10178-5958.

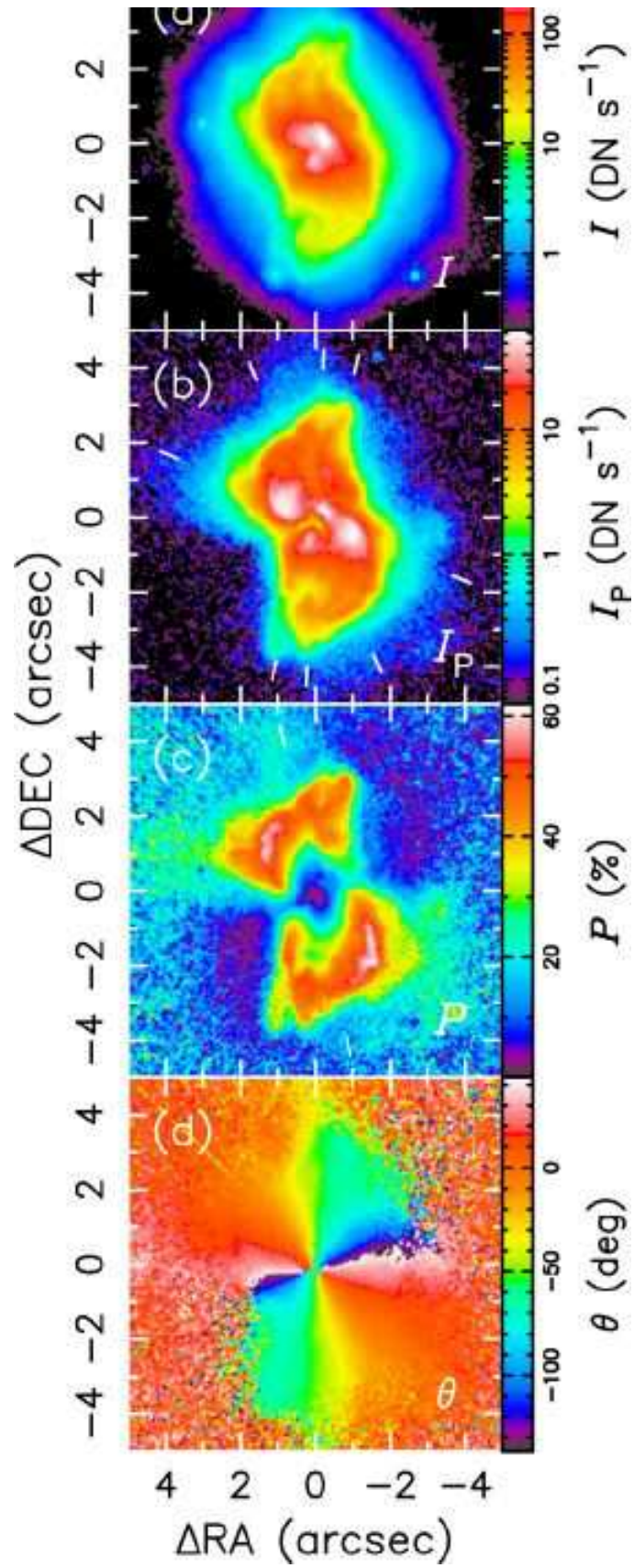


FIG. 5.— Same as Fig. 1, but for IRAS 10197-5750. Radial line segments in the I_P and P maps indicate the directions of possible axes of the shell.

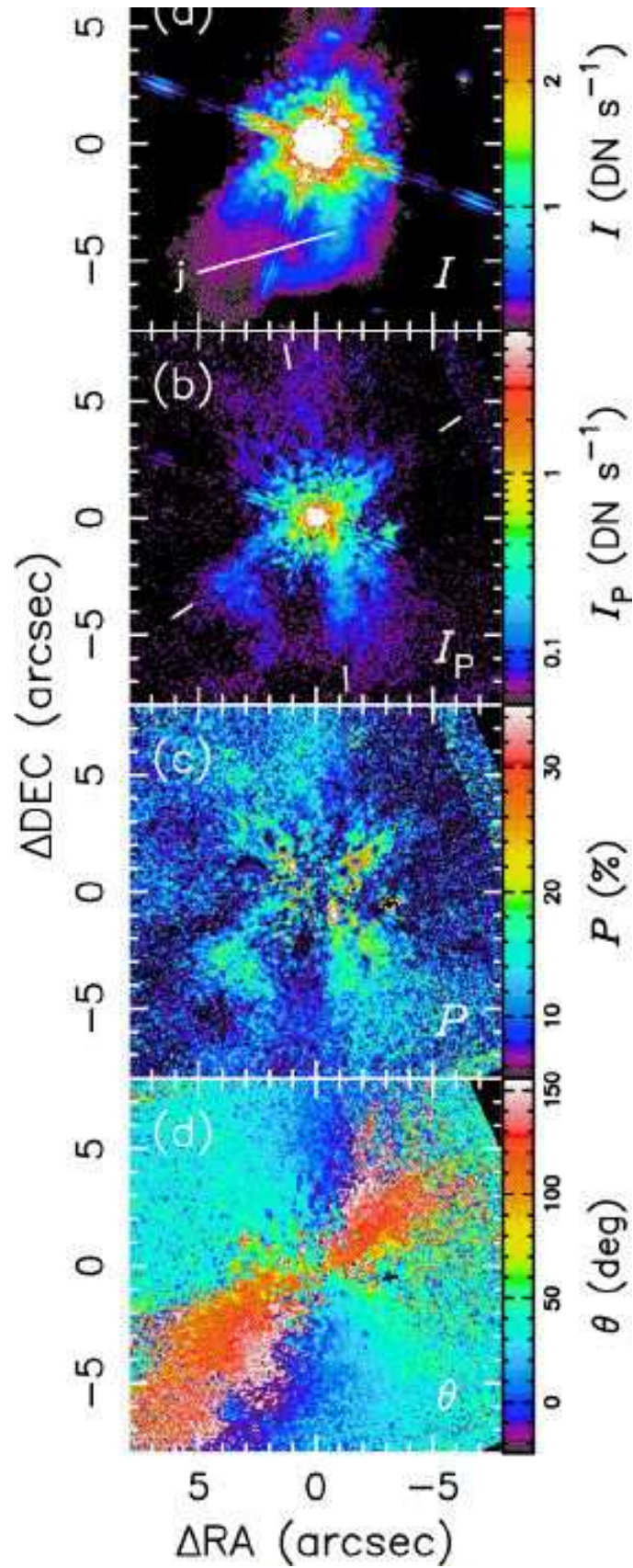


FIG. 6.— Same as Fig. 1, but for IRAS 12419–5414. Radial line segments in the I_P map indicate the directions of the bipolar walls.

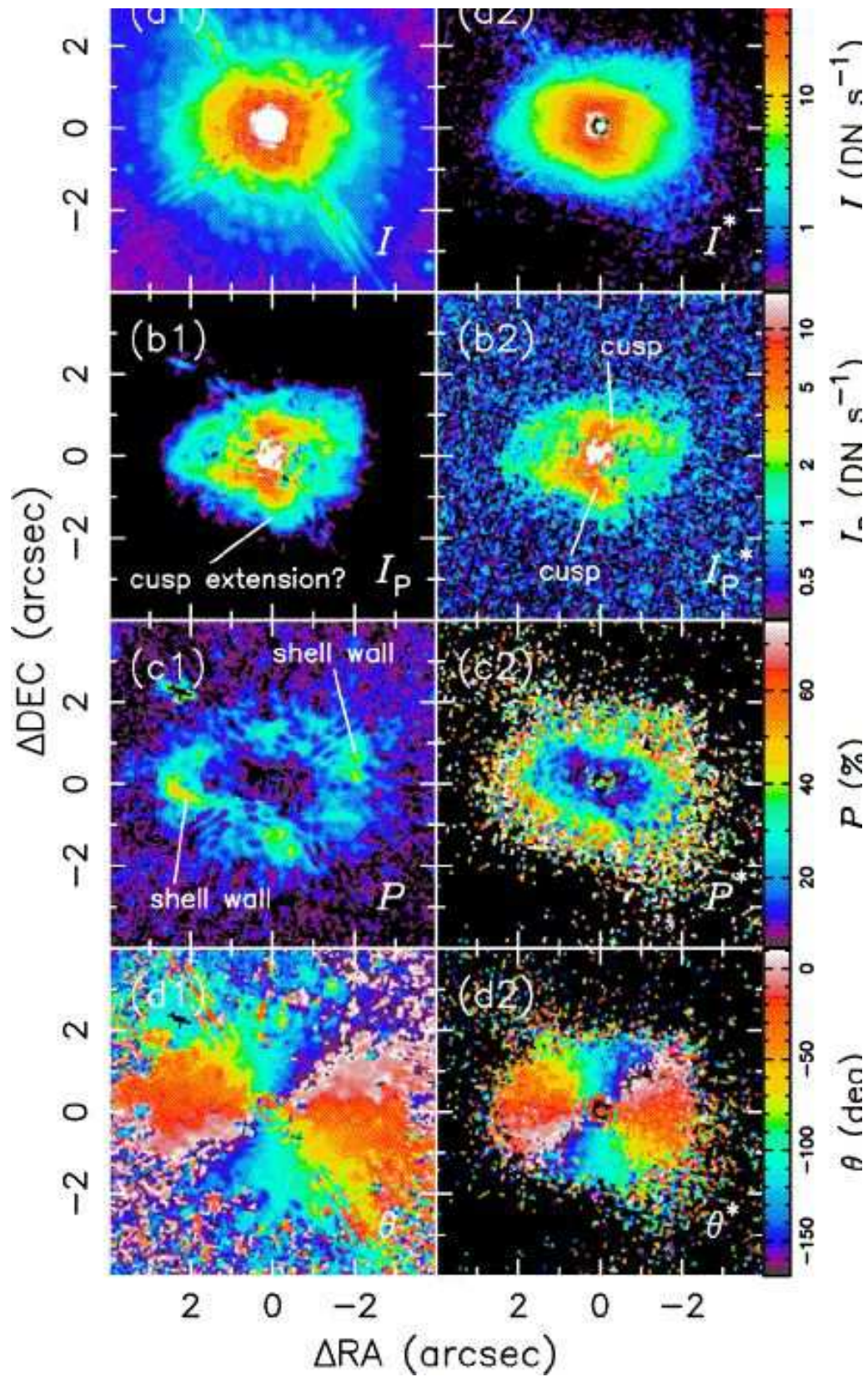


FIG. 7.— Same as Fig. 1, but for IRAS 16594–4656 (Left: original, Right: PSF-subtracted).

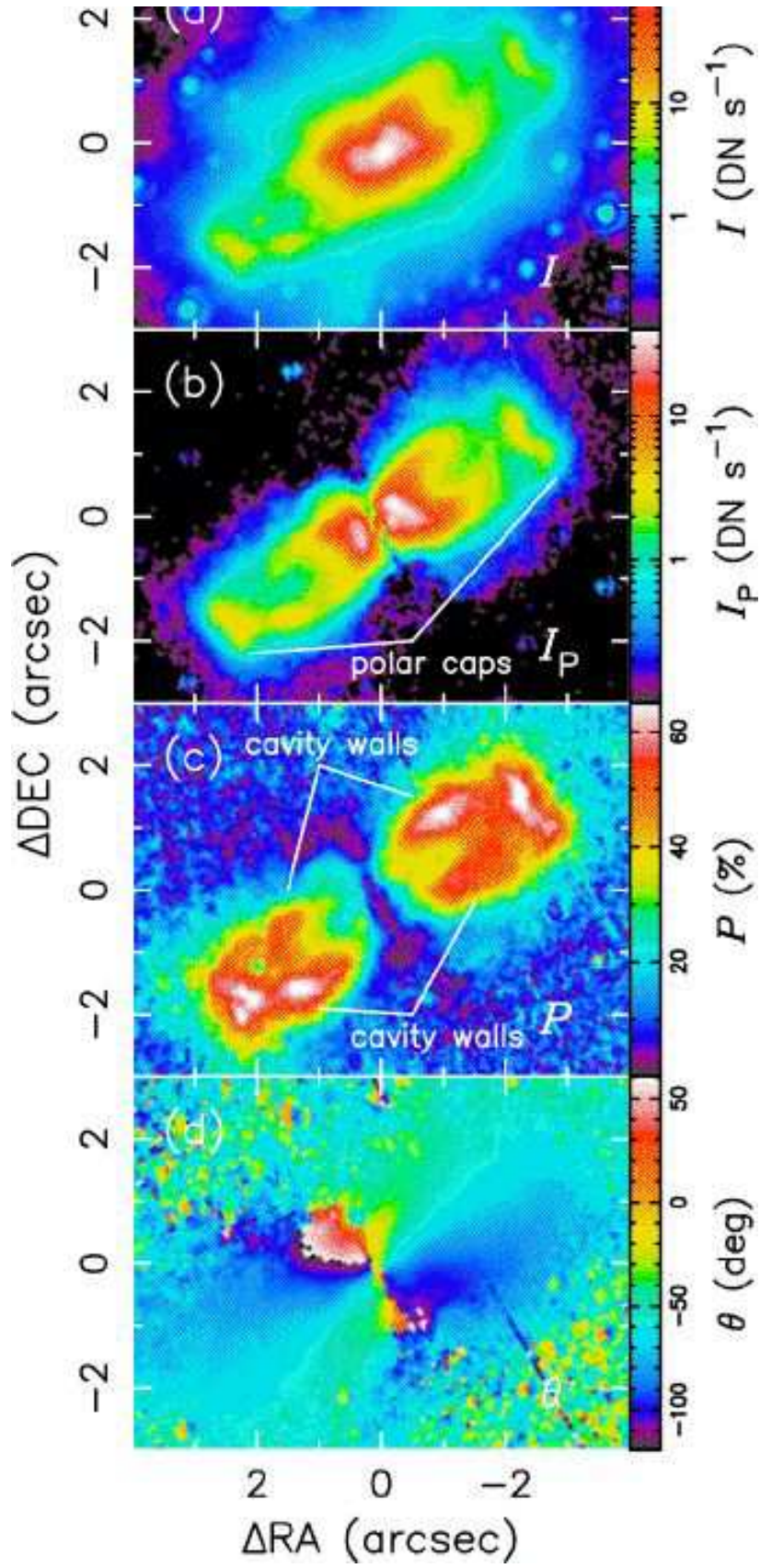


FIG. 8.— Same as Fig. 1, but for IRAS 17150-3224.

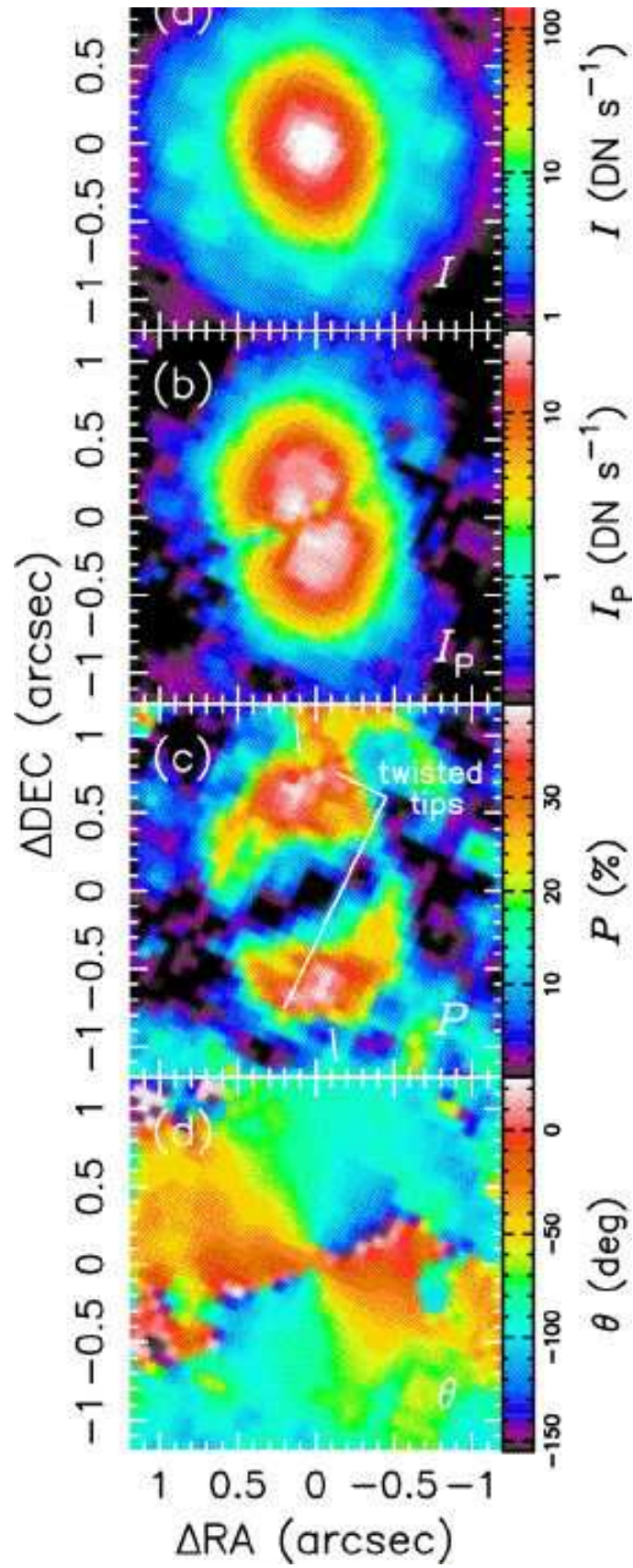


FIG. 9.— Same as Fig. 1, but for IRAS 17245-3951.

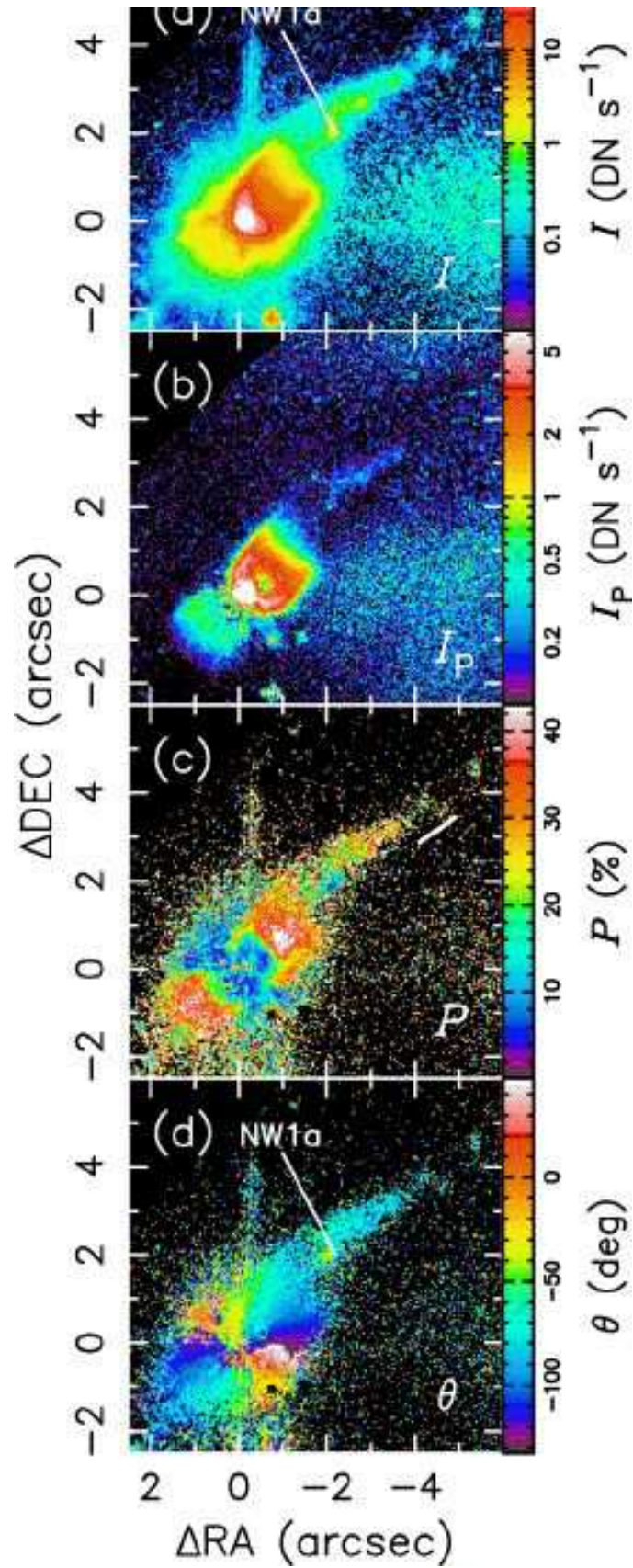


FIG. 10.— Same as Fig. 1, but for IRAS 17423–1755. The position of the NW1a knot (Riera et al. 2003) is shown in the I map. The radial line segment in the P map indicates the orientation of the strong P regions in the bipolar lobes.

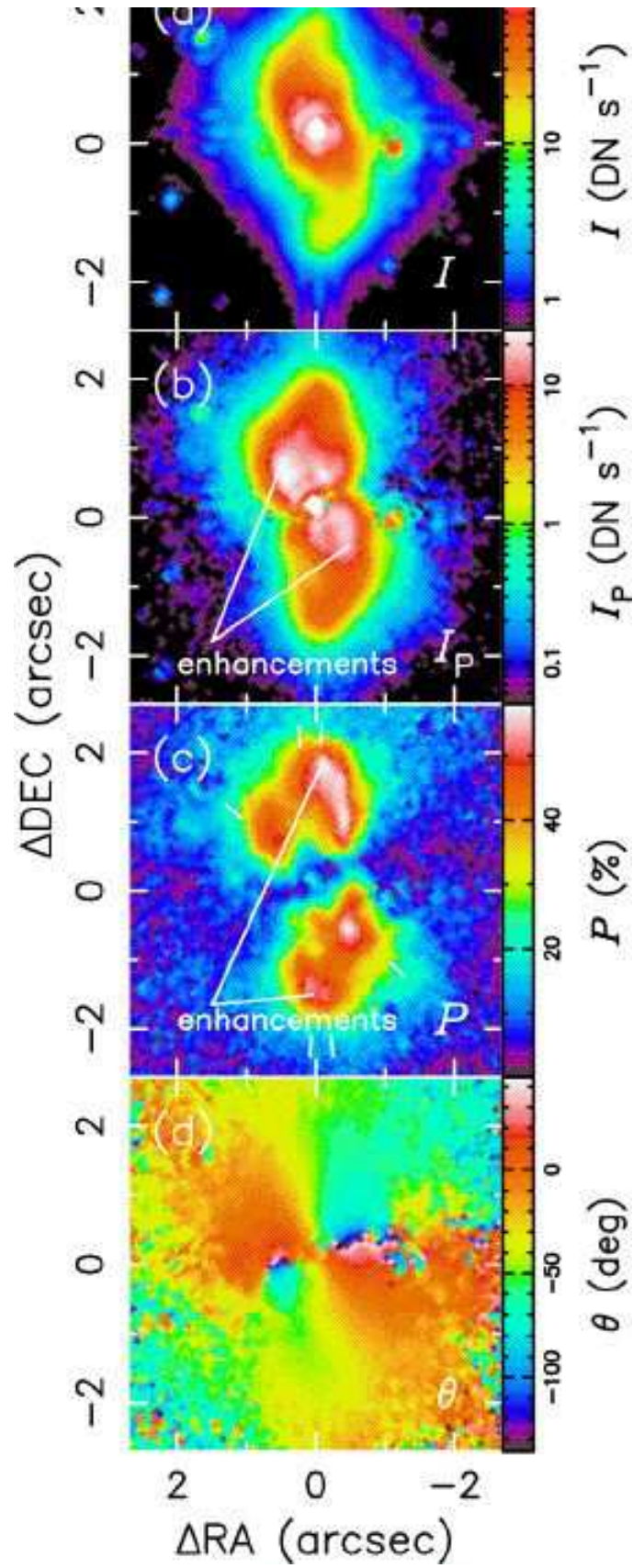


FIG. 11.— Same as Fig. 1, but for IRAS 17441–2411. Radial line segments in the P map indicate the directions of possible axes of the shell.

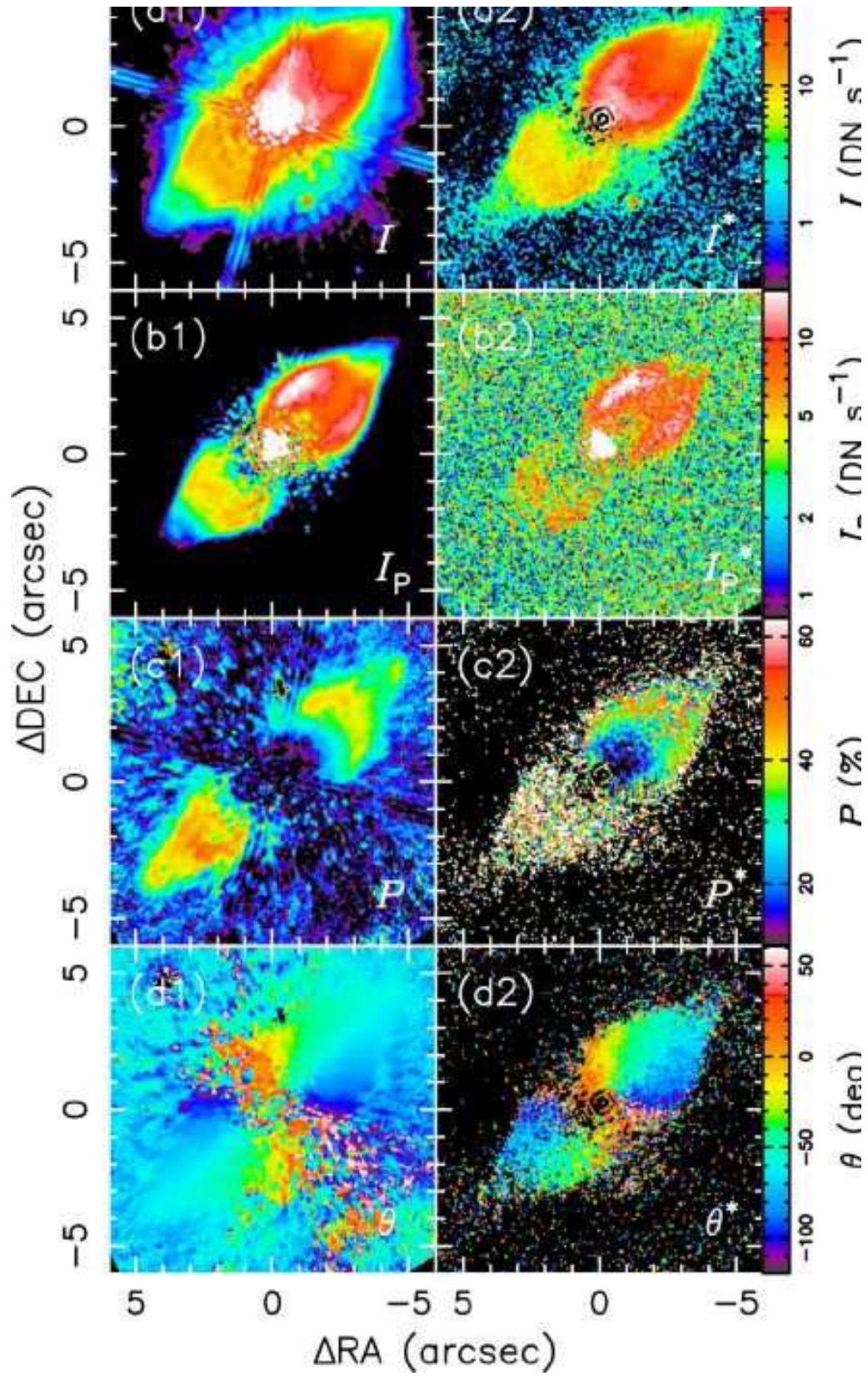


FIG. 12.— Same as Fig. 7, but for IRAS 19343+2926 (Left: original, Right: PSF-subtracted).

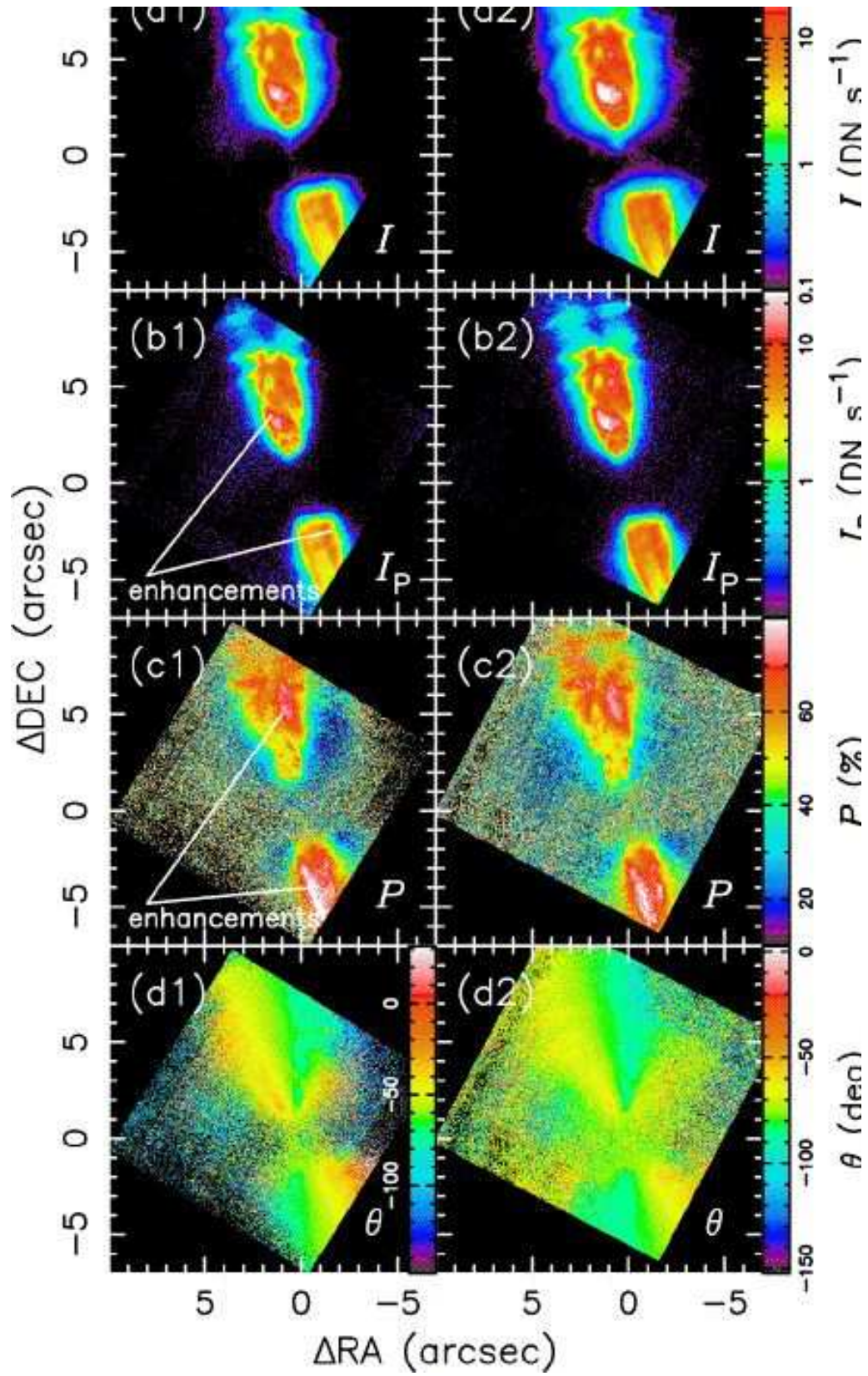


FIG. 13.— Same as Fig. 1, but for the two-epoch observations of AFGL 2688 in the NIC1 band (POL-S; Left: 1998 Apr 8, Right: 2002 Oct 6).

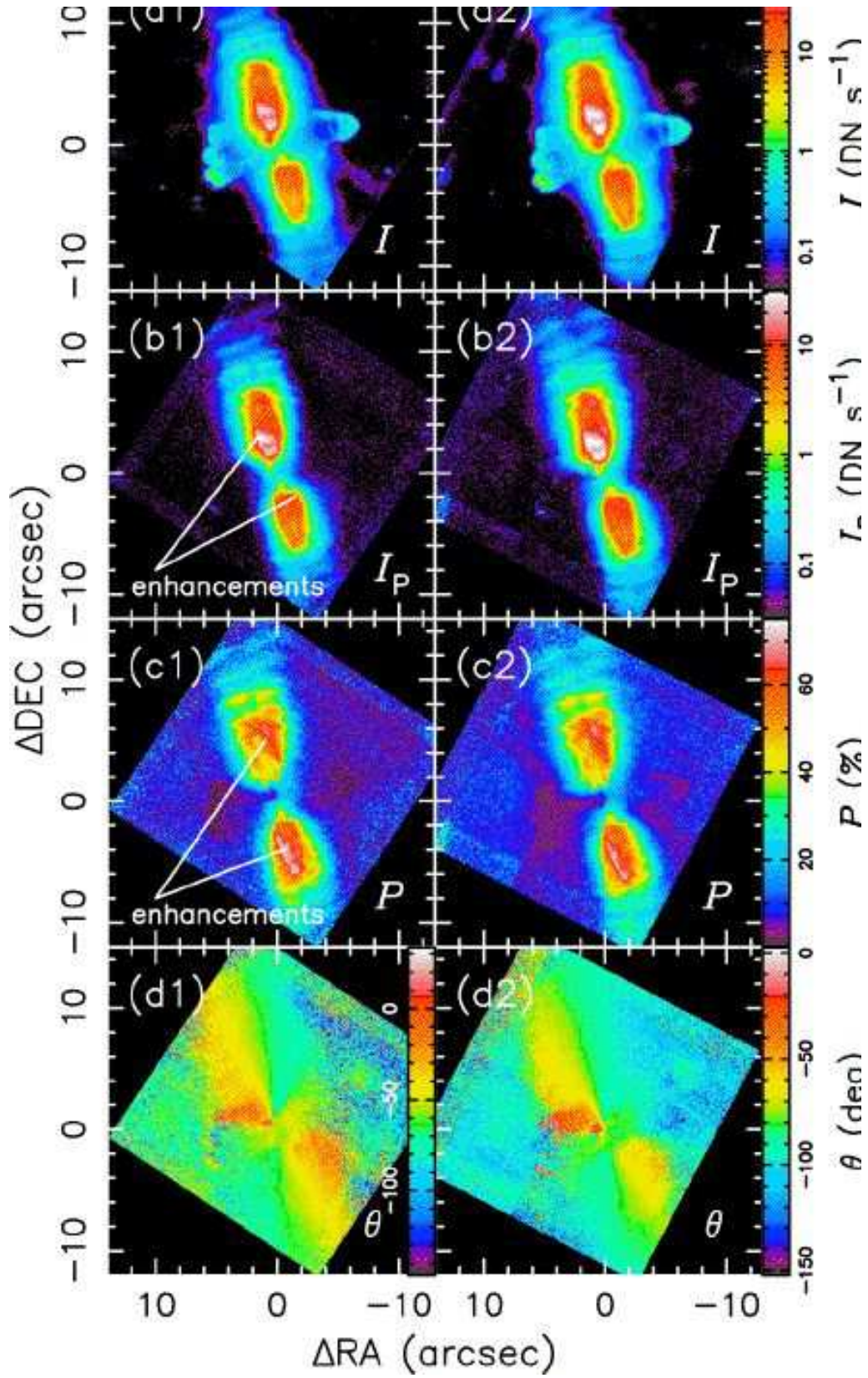


FIG. 14.— Same as Fig. 13, but for the NIC2 band (POL-L) observations.